

Numerical method for binary black hole/neutron star initial data: Code test

Antonios A. Tsokaros¹ and Kōji Uryū²

¹*Department of I.C.S.E., University of Aegean, Karlovassi 83200, Samos, Greece*

²*Department of Physics, University of Wisconsin-Milwaukee, P.O. Box 413, Milwaukee, WI 53201*

(Dated: December 2, 2017)

A new numerical method to construct binary black hole/neutron star initial data is presented. The method uses three spherical coordinate patches; Two of these are centered at the binary compact objects and cover a neighborhood of each object; the third patch extends to the asymptotic region. As in the Komatsu-Eriguchi-Hachisu method, nonlinear elliptic field equations are decomposed into a flat space Laplacian and a remaining nonlinear expression that serves in each iteration as an effective source. The equations are solved iteratively, integrating a Green's function against the effective source at each iteration. Detailed convergence tests for the essential part of the code are performed for a few types of selected Green's functions to treat different boundary conditions. Numerical computation of the gravitational potential of a fluid source, and a toy model for a binary black hole field are carefully calibrated with the analytic solutions to examine accuracy and convergence of the new code. As an example of the application of the code, an initial data set for binary black holes in the Isenberg-Wilson-Mathews formulation is presented, in which the apparent horizons are located using a method described in Appendix A.

I. INTRODUCTION

Inspirational and merger simulations to produce accurate gravitational waveforms are essential for constructing waveform templates for analysis of data from laser interferometric detectors. The ground based interferometers, such as Advanced LIGO or LCGT may detect gravitational waves from the inspiral of $M \sim 10M_{\odot}$ binary black holes within $z \sim 4$, while space based interferometric detectors such as LISA or DECIGO may detect the inspiral of 10^6M_{\odot} supermassive binary black holes, and may discover intermediate mass binary black holes with $M \sim 10^3M_{\odot}$.

Initial data set for binary black holes with a variety of black hole parameters, such as binary mass ratio, and black hole spins, or the binary black hole-neutron star data will become more useful considering the remarkable progress made recently for the inspiraling binary black holes simulations up to a few orbits near the innermost stable circular orbits [1, 2, 3, 4, 5, 6, 7, 8]. Several groups have been achieved to construct binary black hole initial data successfully [9, 10, 11, 12, 13, 14, 15, 16, 17, 18], (for earlier works, see [19]).

In this paper, we introduce a new numerical method suitable for computing accurate initial data sets for binary black holes, black hole-neutron star binaries, and binary neutron star systems. Initial data sets of these kinds are calculated from the Einstein equation written in the form of nonlinear elliptic equations for metric components. Each equation can be written as a Poisson equation with a nonlinear source. Our new Poisson solver is patterned after the Komatsu-Eriguchi-Hachisu (KEH) method [20], widely used to compute rotating neutron stars and more recently to compute, binary neutron stars [21]. The KEH method uses Green's formula to write the field equations in equivalent integral forms and iteratively solve them using spherical coordinates and angular harmonics. The set of equations is discretized by a standard

finite difference scheme.

To extend the method to handle our wider class of binary configurations, we introduce three spherical coordinate patches. Two are centered at each hole and extend outward to a finite radius, larger than the gravitational radius but small enough that the two coordinate patches do not overlap. A third coordinate patch, covering the rest of a spacelike hypersurface, extends to the asymptotic region and overlaps each of the other two patches. There are two important features of our new code: (1) The number of multipoles in the coordinate patch centered at the orbital center can be reduced to $\ell \lesssim 10$ since the sizes of patches for compact objects is extended to about a half of the binary separation. (2) The data between those patches are communicated only at the boundary of those patches to minimize the amount of data to interpolate from one to the other. These novel features result in an efficient code that retains high resolution even near the compact objects where the field is strong. The method has two additional significant advantages: Coding is relatively simple, and the iteration converges robustly.

This paper is organized as follows. In section II, after briefly reviewing the initial value formulation, we introduce our choice of coordinate systems and the formulation of our Poisson solver. Formulas for multipole expansion of Green's function used in the Poisson solver are described in Appendix B. In section III, we describe our numerical methods, including finite differencing and our iteration procedure. In the relating Appendices D and E, the convergence of iteration is discussed further. The results of detailed convergence tests are presented in IV, and an example of binary black hole initial data is displayed in V. The concrete form of the nonlinear elliptic equations for the initial value problem is given in Appendix C, and a method to locate the apparent horizons in the initial data is described in Appendix A.

II. METHOD FOR BINARY BLACK HOLE/NEUTRON STAR INITIAL DATA

Our new numerical method is applicable for various formulations including spatially conformal flat initial data [22], the Isenberg-Wilson-Mathews (IWM) formulation [23, 24, 25], and waveless approximation [26]. We introduce the IWM formulation used for a test calculation of our new code. In this formulation, four constraints and the spatial trace of the Einstein equation are solved, after choosing the trace of the extrinsic curvature and the conformal three metric. We then explain the choice of coordinates and the form of Green's functions used in our version of the KEH method.

A. Formulation

We consider a globally hyperbolic spacetime \mathcal{M} , foliated by a family of spacelike hypersurfaces Σ_t . The binary black hole initial data is constructed on a slice $\Sigma = \Sigma_0$. The unit future-pointing normal to Σ_t will be denoted by $n_\alpha = -\alpha \nabla_\alpha t$ and the metric is written in 3+1 form,

$$\begin{aligned} ds^2 &= g_{\mu\nu} dx^\mu dx^\nu \\ &= -\alpha^2 dt^2 + \gamma_{ij} (dx^i + \beta^i dt)(dx^j + \beta^j dt), \end{aligned} \quad (1)$$

in a chart $\{t, x^i\}$, where $\gamma_{ab}(t)$ is the 3-metric on Σ_t , α the lapse and β^a the shift. The 3-metric γ_{ab} is induced by the projection tensor to the hypersurfaces Σ_t

$$\gamma_{\alpha\beta} = g_{\alpha\beta} + n_\alpha n_\beta. \quad (2)$$

The extrinsic curvature of the foliations is defined by

$$K_{\alpha\beta} = -\frac{1}{2} \mathcal{L}_n \gamma_{\alpha\beta}, \quad (3)$$

where $K_{\alpha\beta}$ satisfies $K_{\alpha\beta} n^\alpha = 0$. With the spatial indices, the spatial tensor $K_{\alpha\beta}$ is written

$$K_{ab} = -\frac{1}{2\alpha} (\partial_t \gamma_{ab} - \mathcal{L}_\beta \gamma_{ab}). \quad (4)$$

Denoting the tracefree part of K_{ab} by A_{ab} and its trace by $K := K_a^a$, we have

$$A_{ab} = K_{ab} - \frac{1}{3} \gamma_{ab} K, \quad (5)$$

and

$$A_{ab} = -\frac{1}{2} \left(\mathcal{L}_n \gamma_{ab} - \frac{1}{3} \gamma_{ab} \gamma^{cd} \mathcal{L}_n \gamma_{cd} \right). \quad (6)$$

\mathcal{L}_n operating to the spatial metric is understood as $\mathcal{L}_n = \frac{1}{\alpha} (\partial_t - \mathcal{L}_\beta)$, where the \mathcal{L}_β is the Lie derivative defined on Σ .

Projecting one index of the Einstein equation normal to the hypersurface Σ , $G_{\alpha\beta} n^\alpha = 0$, yields the Hamiltonian and momentum constraint equations

$$\begin{aligned} 2(G_{\alpha\beta} - 8\pi T_{\alpha\beta}) n^\alpha n^\beta \\ = R - K_{ab} K^{ab} + K^2 - 16\pi \rho_H = 0, \end{aligned} \quad (7)$$

$$\begin{aligned} (G_{\alpha\beta} - 8\pi T_{\alpha\beta}) \gamma^{\beta a} n^\alpha \\ = -D_b (K^{ab} - \gamma^{ab} K) + 8\pi j^a = 0, \end{aligned} \quad (8)$$

where D_a is the covariant derivative on Σ associated with the three metric γ_{ab} . To satisfy the Hamiltonian constraint on a slice Σ , we introduce a conformal decomposition of the spatial metric, $\gamma_{ab} = \psi^4 \tilde{\gamma}_{ab}$, and solve the Hamiltonian constraint for the conformal factor ψ . This prescription leaves the conformal three metric $\tilde{\gamma}_{ab}$ unspecified.

Separating out the trace K , and substituting Eqs. (5) and (6) in the momentum constraint results in an elliptic equation for the shift β^a . The trace, K , remains unspecified. The spatial trace of the Einstein equation,

$$\begin{aligned} (G_{\alpha\beta} - 8\pi T_{\alpha\beta}) \gamma^{\alpha\beta} \\ = 2\mathcal{L}_n K - \frac{1}{2} (R + K^2 + 3K_{ab} K^{ab}) + \frac{2}{\alpha} D_a D^a \alpha - 8\pi S \\ = 0, \end{aligned} \quad (9)$$

can be written as an elliptic equation for the lapse α , once one restricts $\partial_t K$ (e.g., by setting to zero $\partial_t K$ or the derivative of K along a helical Killing vector).

In Appendix C, we show the explicit form of the elliptic equations with nonlinear source for the constraints and the spatial trace of the Einstein equation.

B. Inversion of the Laplacian: Poisson solver

In each component of the field equations a second-order elliptic operator acts on one metric potential. By separating out a flat Laplacian, we write each field-equation component in the form

$$\nabla^2 \Phi = S, \quad (10)$$

where Φ represents a metric potential on a slice Σ . The effective source S involves second derivatives of the metric, but a convergent iteration is possible because they occur in expressions that are $o(r^{-3})$ near spatial infinity. The flat Laplacian ∇^2 is separated in spherical coordinates and inverted by a Poisson solver, and the nonlinear equation (10) is solved iteratively. Our choice of the Poisson solver is to use the Green's formula, an integral form of Eq. (10). Using the Green's function of the Laplacian

$$\nabla^2 G(x, x') = -4\pi \delta(x - x'), \quad (11)$$

where x and x' are positions, $x, x' \in V \subseteq \Sigma$, the Green's formula is written

$$\Phi(x) = -\frac{1}{4\pi} \int_V G(x, x') S(x') d^3 x'$$

$$+\frac{1}{4\pi} \int_{\partial V} [G(x, x') \nabla'^a \Phi(x') - \Phi(x') \nabla'^a G(x, x')] dS'_a. \quad (12)$$

This formula is valid for any connected space V as long as each term is integrable. The function $G(x, x')$ is a sum of a Green's function without boundary and a homogeneous solution $F(x, x')$ to the Laplace equation,

$$G(x, x') = \frac{1}{|x - x'|} + F(x, x'), \quad (13)$$

which satisfy

$$\nabla^2 \frac{1}{|x - x'|} = -4\pi \delta(x - x'), \quad (14)$$

$$\nabla^2 F(x, x') = 0. \quad (15)$$

Eq. (12) is a formal solution to the Poisson equation (10) for any $G(x, x')$ that satisfies Eq. (11), even if the source S depends on the field Φ nonlinearly. Thereby, the elliptic equation with a nonlinear source can be solved iteratively using Eq. (12). We call this iteration the KEH iteration hereafter.

With the surface term included, Eq. (12) is an identity, valid for any choice of Green's function. Requiring convergence of the KEH iteration, however, imposes the following key restrictions on that choice: For solving a Dirichlet problem, no multipole component of $\nabla'^a G(x, x')$ can vanish on the entire boundary; similarly, for solving a Neumann problem, no multipole component of $G(x, x')$ can vanish on the entire boundary. As long as the Green's function satisfies this restriction, it is not necessary to construct $F(x, x')$ appropriate for each boundary condition; for example, the Green's function without boundary term $1/|x - x'|$ can be used for the Neumann problem.

A reason to use the Poisson solver Eq. (12) is tied to the facts that the spherical coordinates (r, θ, ϕ) are suitable for constructing numerical domains for binary black holes and neutron stars, and that one can use a multipole expansion of the Green's function in these coordinates. The Poisson solver turns out to be simple for coding, CPU inexpensive and accurate as shown in Sec.IV. In the rest of this section, we introduce numerical domains for the binary black holes, and discuss the choice of the Green's function.

C. Construction of the computational domain

To describe the binary black hole/neutron star data, we introduce three spherical domains. Two small domains are centered at the two compact objects surrounding them, while the third domain partly covers the first two and extends to the asymptotic region. The large domain is not necessarily positioned at the center of mass of the two compact objects. These domains are shown schematically in Fig. 1. In this section, we consider the

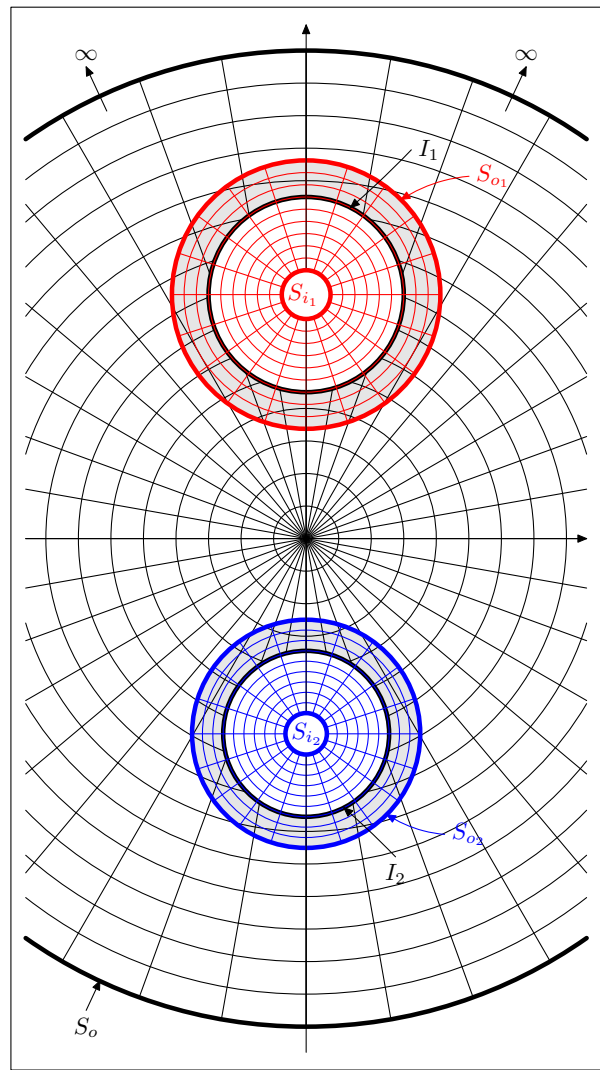


FIG. 1: The computational domain. One central grid and two black hole grids with excised regions.

binary black hole case as an example, and refer to the domains around the compact objects as the black hole coordinate system (BHCS) and the third one as the central coordinate system (CCS).

CCS extends to the asymptotic region; practically the radius r of the sphere S_o is set large enough that the multipoles of order r^{-2} and higher are negligible. It excludes the interiors of the two spheres I_1 and I_2 , which are centered at each black hole, and whose radii are taken larger than the gravitational radius of each hole but not as large as to intersect each other. Therefore, in the domain of CCS, Eq. (12) involves (1) the surface integrals over a large sphere S_o where the asymptotic condition of each field variable is imposed, (2) the interfaces I_1 and I_2 , and (3) the volume integral of the source term S between these three spheres.

The first black hole computational domain BHCS-1 extends from a sphere S_{i1} to S_{o1} , both centered at the black

hole, and the second one BHCS-2 from S_{i_2} to S_{o_2} . The region inside S_{i_1} and S_{i_2} is excised from the computational domain. The code allows the option of dispensing with the inner boundary, for a black hole; and for a neutron star the inner boundary is never used (in this case in the BHCS the minimum value of r is zero). Note that the spheres I_1 , S_{i_1} , and S_{o_1} are concentric, and the same for I_2 , S_{i_2} , and S_{o_2} .

The boundaries I_1 , I_2 , S_{o_1} , and S_{o_2} are introduced to reduce the number of terms in the Legendre expansion of the Green's function (B1) in CCS. Taking the radii of I_1 and I_2 large enough, the contribution of higher multipoles in CCS is included in the surface integrals over I_1 and I_2 . Because of this, a small number of multipoles, typically $\ell \lesssim 10$, is enough to resolve the volume integral of CCS. Thus by increasing the radial resolution in BHCS where the metric potentials may vary rapidly, we can compute an accurate solution without having a high resolution in CCS.

Between concentric spheres I_1 and S_{o_1} of BHCS-1, and I_2 and S_{o_2} of BHCS-2, we reserve overlapping regions, which appear shaded in Fig. 1. These interfaces I_i and S_{o_i} ($i = 1$ or 2) are not physical boundaries; the boundary conditions of the fields are not prescribed there. Instead, the value of the field on I_i is calculated from the field on BHCS, and the value of the field on S_{o_i} from the field on CCS, thus resulting to a smooth potential field throughout BHCS and CCS that satisfies the physical boundary conditions at the BH boundary and the asymptotic region. The significance of the overlap region is to decrease the number of iterations to convergence. A toy model of this iteration procedure is explained in Appendix D.

D. Choices for the Green's function

In Sec. II B, we discussed a restriction on the choice of Green's function due to the KEH iteration using Eq. (12). Any Green's function that meets this restriction can be used in the Poisson solver (12). The Green's functions are expanded in multipoles over the spherical coordinates (r, θ, ϕ) of each domain. Explicit formulas for the expansions are shown in Appendix B. In actual numerical computations, the summation of multipoles in ℓ is truncated at a certain finite number L , for which we typically choose $L \sim 10$ in order to resolve the deformation of the field Φ .

For CCS, we choose the Green's function without boundary

$$G^{\text{NB}}(x, x') = \frac{1}{|x - x'|}, \quad (16)$$

which has the simplest form and picks up the contributions from the interfaces I_1 and I_2 . In the volume integral of Eq. (12) over the domain outside of spheres I_1 and I_2 , and inside of S_o , the function $G^{\text{NB}}(x, x')$ is expanded in multipoles over the spherical coordinates of CCS. For

the surface integrals on I_1 and I_2 , $G^{\text{NB}}(x, x')$ is expanded in multipoles over the spherical coordinates of BHCS-1 and BHCS-2 respectively. Therefore, the position x corresponding to each grid point of CCS is labeled by the spherical coordinates of BHCS, not CCS, in these surface integrals.

For BHCS, when the excision of the computational domain is not used at the black hole, G^{NB} will be chosen. However when the computational region is excised inside a sphere S_{i_1} and S_{i_2} , G^{NB} can not be used for the Dirichlet problem. As shown in Appendix E, the $\ell = 0$ component of $\nabla'^a G^{\text{NB}}(x, x')$ becomes zero at the inner boundary sphere, and hence it can not pick up Dirichlet data there during the iteration of Eq. (12). When the black hole boundary condition for a certain field is given by Dirichlet data, we choose the Green's function for the Dirichlet problem between two concentric spheres G^{DD} given in Appendix B 2. When Neumann data is imposed at the black hole boundary, the Green's function without boundary G^{NB} may be used. We also coded the Green's function between two concentric sphere G^{ND} for which the Neumann condition is imposed at the inner boundary of BHCS S_{i_1} and S_{i_2} , and the Dirichlet data at the outer boundary of BHCS S_{o_1} and S_{o_2} .

III. METHOD FOR NUMERICAL COMPUTINGS

A. Grid spacing

Hereafter, coordinate labels (r, θ, ϕ) will be used for all three spherical coordinate systems, CCS, BHCS-1, and BHCS-2 unless otherwise stated. We introduce three spheres, S_a , S_b , and S_c at $r = r_a$, $r = r_b$, and $r = r_c$ respectively, such that $r_a < r_c < r_b$, in each coordinate system. The sphere S_a is used as an inner boundary for BHCS when the excision boundary is used, which corresponds to S_{i_1} and S_{i_2} in Fig. 1. For CCS or BHCS without excision, the radius $r_a = 0$ is understood. The sphere S_b is the outer boundary of each coordinate system that corresponds to S_o , S_{o_1} , and S_{o_2} in the same figure. The sphere S_c is located between S_a and S_b where we change the grid spacing in the radial coordinate.

The code is constructed to handle non-equidistant grid spacing in each coordinate grid. In CCS, the grid starts with equidistant spacing from the origin $r = 0$ to a sphere S_c , and from there it becomes non-equidistant with an ever increasing spacing up to the outer boundary S_b . The black hole grids are equidistant from their outer boundaries S_b down to S_c , and from that point until the inner boundary S_a they become non-equidistant with an ever decreasing spacing. For the black hole grids, finer grids are adequate to have an accurate representation of the rapidly varying fields near the hole, while further away, where the potentials are changing slowly, larger spacing can be used without compromising accuracy.

We summarize common notations for all three coordi-

nate systems as follows;

r_a : Radial coordinate where each grid starts.

r_b : Radial coordinate where each grid finishes.

r_c : Radial coordinate between r_a and r_b where each grid changes from equidistant to non-equidistant or vice versa.

N_r : Total number of intervals Δr_i between r_a and r_b .

n_r : Number of intervals Δr_i between r_a and r_c .

n_v : Number of overlapping intervals of BHCS to CCS.

N_θ : Total number of intervals $\Delta\theta_i$ for $\theta \in [0, \pi]$.

N_ϕ : Total number of intervals $\Delta\phi_i$ for $\phi \in [0, 2\pi]$.

d : the separation between centers of BHCS and CCS.

In particular, we use the following setup for the grid spacings.

Central Grid

$$\Delta r_i = \Delta h = \frac{r_c - r_a}{n_r} \quad \text{for } 1 \leq i \leq n_r$$

$$\Delta r_{i+1} = k\Delta r_i \quad \text{for } n_r \leq i \leq N_r - 1$$

where $k > 1$. Then we have

$$r_b - r_c = \Delta h \frac{k - k^{N_r - n_r + 1}}{1 - k}. \quad (17)$$

Given r_a , r_b , r_c , N_r , and n_r this is the equation that will give us the spacing factor k for the central grid. Note that for the central grid, $r_a = 0$.

Black Hole Grids (I and II)

$$\Delta r_i = \Delta h = \frac{r_b - r_c}{N_r - n_r} \quad \text{for } n_r + 1 \leq i \leq N_r$$

$$\Delta r_i = k\Delta r_{i+1} \quad \text{for } 1 \leq i \leq n_r$$

where $k < 1$. Then we have

$$r_c - r_a = \Delta h \frac{k - k^{n_r + 1}}{1 - k}. \quad (18)$$

For the angular θ and ϕ spacings for all three coordinate systems, we usually take equidistant grid spacing.

B. Finite differencing

Standard finite difference scheme is applied to evaluate the derivatives of the sources and their numerical integrals in Eq. (12). The derivatives of source terms are calculated using fourth order Lagrange formula, and the integrals using either trapezoidal rule or fourth order Simpson rule in θ and ϕ coordinates and second order mid-point rule for the r coordinate. For the surface integrals at the interfaces S_{o1} and S_{o2} in Fig. 1, the field and its derivatives are evaluated from the nearby 64 points of CCS as shown in Fig. 2 (a point A on S_{o_i}), to which the fourth order interpolation is applied.

C. Iteration procedure

The KEH method at the n -th iteration follows the procedure,

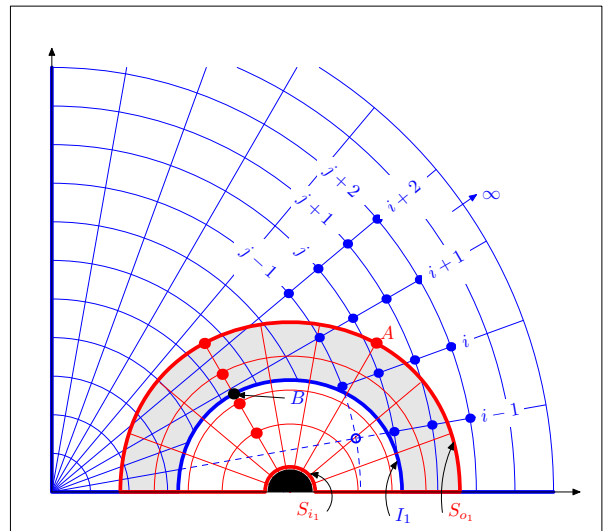


FIG. 2: Schematic figure for computational domain with overlapping grids.

- 1) Compute all the source terms in Eq. (12).
- 2) Call the Poisson Solver (described below) for each of the variables and compute their new values $\Phi^{(n)}$.
- 3) Compare these newly computed values $\Phi^{(n)}$ with those of previous iteration $\Phi^{(n-1)}$.
 - If the difference is less than your accepted error \Rightarrow **convergence**
 - If not, update $\Phi^{(n)}$, according to

$$\Phi^{(n)} := c\Phi^{(n)} + (1 - c)\Phi^{(n-1)}, \quad (19)$$

and go back to step (1).

We conclude convergence of the iteration when the difference between two successive iterations becomes small as defined by

$$\frac{2|\Phi^{(n)} - \Phi^{(n-1)}|}{|\Phi^{(n)}| + |\Phi^{(n-1)}|} < \epsilon_c, \quad (20)$$

where $\epsilon_c = 10^{-8}$ is taken in typical calculations. The iteration usually converges successfully, taking the convergence factor c to be around 0.5 when a fluid source is present. For the binary black hole case, it is even possible to achieve convergence with the factor $c = 1$.

The Poisson Solver for a potential at the n th iteration performs the following sequence of instructions :

- 1) Compute the potential and its radial derivative at the outer boundary of the black hole grid by interpolating from nearby points of the central grid.
- 2) Compute the surface integrals at the outer boundaries of the black hole grids by using the potential and its derivative from step (1).

- 3) Compute the surface integrals at the inner boundaries of the black hole grids by using the boundary conditions for the potential or its derivative.
- 4) Compute the volume integrals inside the black hole grids. Add the contributions from steps (2) and (3), to obtain the value of the potential inside the black hole grids.
- 5) Interpolate using points of the black hole grids to compute the potential and its derivative on the interfaces I_1 and I_2 of the central grid.
- 6) Compute the surface integrals on I_1 and I_2 by using results from step (5).
- 7) Compute the surface integral at the outer boundary of the central grid by using the boundary conditions for the potential or its derivative.
- 8) Compute the volume integral inside the central grid. Add the contributions from steps (6) and (7), to obtain the value of the potential inside the central grid.

IV. CODE TEST

In this section, we show the results for the convergence test of our new code. In the first test we compute the Newtonian potential of two spherical masses. Then we compute simple models for time symmetric black hole data.

As mentioned in the previous section, the local truncation errors of the finite differencing used in our code are of order $O(\delta r^2)$, $O(\delta\theta^4)$, and $O(\delta\phi^4)$ in each coordinate. Also we have a truncation error from multipoles higher than $L \sim 10$. Since the local truncation error at each grid point is a linear combination of these, and because of the excision used in CCS, we find a non-uniform convergence of relative errors as we increase the resolution, as well as a non-uniform distribution of the errors in space, as shown below. However, overall convergence is faster than second order for all cases with a fixed L .

A. Convergence test for the Newtonian potential

1. Set up for the test problem

The Poisson equation (10) with a spherical source of the form

$$S(r) = \begin{cases} \frac{(R^2 - r^2)^2}{R^4} & \text{if } 0 \leq r \leq R, \\ 0 & \text{if } r > R, \end{cases} \quad (21)$$

Type	Coordinate	r_a	r_b	r_c	d	N_r	n_r	n_v	N_θ	N_ϕ	L
S1	CCS	0	100	3	—	80	40	—	20	80	10
	BHCS-1	0	1.25	0	1.5	30	0	6	10	40	5
S2	CCS	0	100	3	—	160	80	—	40	160	10
	BHCS-1	0	1.25	0	1.5	60	0	12	20	80	5
S3	CCS	0	100	3	—	320	160	—	80	320	10
	BHCS-1	0	1.25	0	1.5	120	0	24	40	160	5

TABLE I: Coordinate parameters, and the number of grid points for each coordinate system with different resolutions. Each resolution is double the one above. The parameters for BHCS-2 are identical to those of BHCS-1. L is the highest multipole included in the Legendre expansion.

has the solution

$$\Phi = \begin{cases} -\frac{R^2}{6} \left[1 - \left(\frac{r}{R}\right)^2 + \frac{3}{5} \left(\frac{r}{R}\right)^4 - \frac{1}{7} \left(\frac{r}{R}\right)^6 \right] & \text{if } 0 \leq r \leq R \\ -\frac{8R^3}{105r} & \text{if } r \geq R \end{cases} \quad (22)$$

where r is the radial coordinate and R a constant.

The source (21) is centered at each BHCS-1 and BHCS-2, whose positions in CCS are $(r, \theta, \phi) = (1.5, \pi/2, 0)$ and $(1.5, \pi/2, \pi)$, and the radii of BHCS-1 (S_{o_1}) and 2 (S_{o_2}), extend up to $r_b = 1.25$. The radii of the excised spheres in CCS I_1 and I_2 are taken as $r = 1.0$. The radial coordinate r of CCS is equidistant until $r_c = 3$ and from that point until $r_b = 100$ is non-equidistant, while the BHCSs are equidistant in the radial coordinate. The exact potential of two sources is a superposition of solutions (22) centered at each of the two BHCS. For the boundary condition at $r = 100$ in CCS, we put the potential to have its exact value. The KEH iteration explained in previous sections is applied to calculate the potential Φ until convergence is made.

2. Accuracy of numerical solutions

In Fig. 3, we show, for two cases, the percentage of the relative error between the numerical and exact solution,

$$\left| \frac{\delta\Phi}{\Phi} \right| [\%] := 100 \left| \frac{\Phi_{\text{exact}} - \Phi_{\text{numerical}}}{\Phi_{\text{exact}}} \right|. \quad (23)$$

In the first case (top panel), the radius of the source R is $R = 0.5$, which is smaller than the boundary radius $r_b = 1.25$ of BHCS-1 and BHCS-2. For the second case (bottom panel), the source radius $R = 1.4$ is taken so that the sources extend to CCS. The error is plotted along the radial coordinate at $(\theta, \phi) = (\pi/2, 0)$ (see Fig. 1). Along this line (labeled x in the figures) BHCS-1 extends from $x = 0.25$ to 2.75 , the source (for $R = 1.4$) from $x = 0.1$ to 2.9 , and overlap of CCS and BHCS-1 from $x = 0.25$ to 0.5 and from 2.5 to 2.75 in CCS. The errors in the interval $x \in [0, 4]$ are shown in the plots.

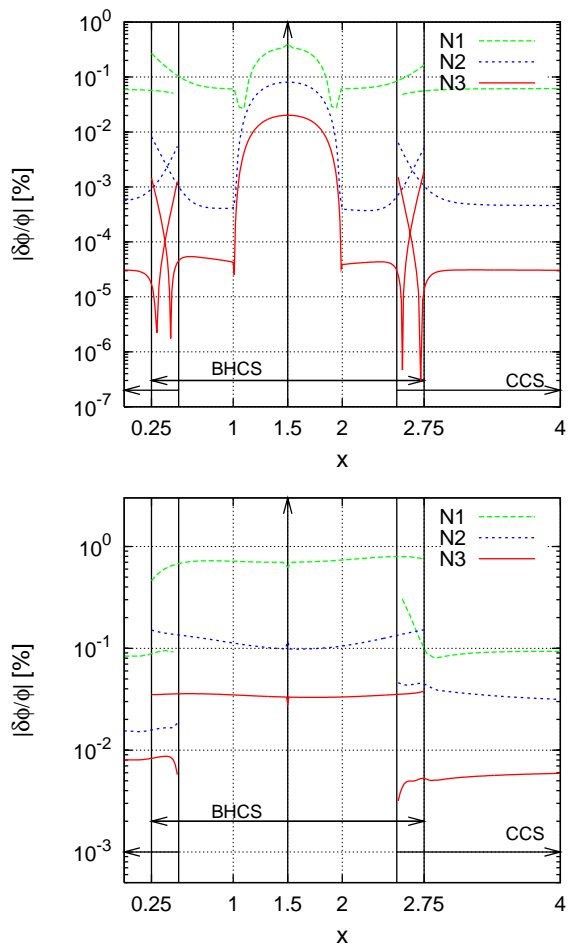


FIG. 3: Percentage of relative error for the source of type (21) for three different resolutions. Each line from top to bottom corresponds to the resolutions S1, S2, and S3 in table I. Vertical lines are the location of the boundary of numerical domains. Top panel: The source is inside BHCS, $R = 0.5 < r_b = 1.25$. Bottom panel: The source extends outside of the BHCS, $R = 1.4 > r_b = 1.25$.

In Fig. 3, the resolution doubles from the top to bottom (dashed, dotted, and solid) lines in each panel whose parameters are shown in Table I. The errors of the lowest resolution, top lines in each panel of Fig. 3, are fairly small. For the case with $R = 0.5$ in the top panel, the error drops 1/4 near the center of the source as we double the resolution, which shows the second order convergence. For the case of larger source in the bottom panel, the volume integration in CCS introduces a truncation error that behaves differently from the former case. Regardless of that the error drops again roughly as 1/4.

It is remarkable that the potential of such binary sources can be accurately computed with the small number of multipoles as $L = 10$ in CCS. In previous work [21], for binary neutron stars, in which only one domain corresponding to CCS was used to compute the field, a summation of more than 30 multipoles was required to obtain an accuracy of order 0.01% (regarding the relative

errors) that we obtain here.

3. Convergence property of iterations

In test problems presented in this section, the number of iterations required to achieve convergence is about 10-20. Generally convergence can be accelerated using (1) a good initial guess for starting the iteration, and (2) a carefully chosen convergence factor c in Eq. (19).¹ If the source is very steep and the convergence factor large (near 1.0) the iteration could blow up instead of converge. The number of iterations also depends critically on the size of the overlap region between the surfaces S_{o_i} and I_i ($i = 1, 2$) (see Appendix D). For the results shown in Fig. 3, in which the overlap is 20% of the radii of S_{o_i} , the solution is evaluated after 14 iterations with a convergence factor $c = 0.8$, starting from a constant (zero) potential. For this problem, we can achieve convergence with a convergence factor $c = 1.0$ in 11 iterations with the same overlap region. On the other hand, when the overlap is set about 2.4% of the radii of S_{o_i} , the iteration does not converge with $c = 0.8$, and it does for $c = 0.1$ after 168 iterations. Although the larger overlap region is favourable for having the number of iteration smaller, the radii of I_i has to be taken large enough to keep the number of multipoles used in CCS small. Our choice for the radii of S_{o_i} and I_i meets these two requirements.

We also observed that our method produces the same solution irrespective of the value of the convergence factor, in the above range $0.1 \leq c \leq 1$, as long as the iteration converges.

B. Convergence test for solutions with excision boundaries

1. Analytic solutions

To test our elliptic solver for the case with black hole excision boundaries, we consider the following simple solutions which model one or two black holes. For the metric

$$ds^2 = -\alpha^2 dt^2 + \psi^4 f_{ij} dx^i dx^j, \quad (24)$$

where f_{ij} is the flat metric, the hamiltonian constraint and the spatial trace of the Einstein equation $G_{\alpha\beta}\gamma^{\alpha\beta} = 0$, give

$$\nabla^2 \psi = 0 \quad \text{and} \quad \nabla^2 (\alpha \psi) = 0. \quad (25)$$

¹ When one iterates the fluid variables together with the gravitational fields, such as a computation for binary neutron star equilibrium, the number of iteration may increase as many as a few hundreds.

These equations have solutions,

$$\psi = 1 + \frac{M}{2r} \quad \text{and} \quad \alpha\psi = 1 - \frac{M}{2r}, \quad (26)$$

which correspond to the Schwarzschild solution with mass M , in isotropic coordinates, $\psi|_{r \rightarrow \infty} = 1$, and $\alpha|_{r \rightarrow \infty} = 1$.

We compute the solution (26) numerically by imposing boundary conditions at the sphere $r_a = M/2$. In order to test the code using Dirichlet boundary conditions, we set the boundary value at $r = r_a$ to the exact value computed from (26). For testing Neumann boundary condition, we take the value of the derivative of (26).

For example, the Neumann condition for $\alpha\psi$ becomes

$$\frac{\partial(\alpha\psi)}{\partial r} = \frac{M}{2r^2} \quad \text{at} \quad r = \frac{M}{2}. \quad (27)$$

Note that the method of images, [27], is identical to requiring that ψ satisfy the Robin boundary condition

$$\frac{\partial\psi}{\partial r} + \frac{\psi}{2r} = 0 \quad \text{at} \quad r = M/2. \quad (28)$$

The boundary condition for the lapse,

$$\alpha = 0, \quad (29)$$

yields the solution (26), antisymmetric about $r = r_a$.

One can also construct a two black hole solution that satisfies imaging conditions (28) and (29) at two spheres [27]. Instead of using solutions of this kind, we use the Brill-Lindquist solution [28] to Eq. (25) which is sufficient for the purpose of our code test. Writing coordinates of BHCS-1 with subscript 1 and BHCS-2 with subscript 2, we write a two black hole solution to Eq. (25),

$$\psi = 1 + \frac{M_1}{2r_1} + \frac{M_2}{2r_2} \quad \text{and} \quad \alpha\psi = 1 - \frac{M_1}{2r_1} - \frac{M_2}{2r_2}. \quad (30)$$

We set the radii of excision boundaries at $r_1 = M_1/2$ and $r_2 = M_2/2$, and impose either the Dirichlet boundary condition, which is given by the values of Eq. (30) at the boundaries, or the Neumann boundary condition, which assigns the values of the derivatives of ψ and $\alpha\psi$ as

$$\frac{\partial\psi}{\partial r_1} = -\frac{M_1}{2r_1^2} - \frac{M_2}{2r_2^2} \frac{\partial r_2}{\partial r_1} \quad \text{at} \quad r_1 = \frac{M_1}{2}, \quad (31)$$

$$\frac{\partial(\alpha\psi)}{\partial r_1} = \frac{M_1}{2r_1^2} + \frac{M_2}{2r_2^2} \frac{\partial r_2}{\partial r_1} \quad \text{at} \quad r_1 = \frac{M_1}{2}, \quad (32)$$

and $1 \leftrightarrow 2$ for the boundary at $r_2 = M_2/2$. The coordinates r_1 and r_2 are written in terms of each other as

$$r_1 = \sqrt{r_2^2 - 2r_2 a \sin \theta_2 \cos \phi_2 + a^2}, \quad (33)$$

$$r_2 = \sqrt{r_1^2 + 2r_1 a \sin \theta_1 \cos \phi_1 + a^2}. \quad (34)$$

One black hole data without source											
Type	Coordinate	r_a	r_b	r_c	d	N_r	n_r	n_v	N_θ	N_ϕ	L
N1	CCS	0	100	3	—	80	40	—	20	80	10
	BHCS-1	0.02	1.25	0.02	1.5	30	0	6	10	40	5
	BHCS-2	0	1.25	0	1.5	30	0	6	10	40	5
N2	CCS	0	100	3	—	160	80	—	40	160	10
	BHCS-1	0.02	1.25	0.02	1.5	60	0	12	20	80	10
	BHCS-2	0	1.25	0	1.5	60	0	12	20	80	10
N3	CCS	0	100	3	—	320	160	—	80	320	10
	BHCS-1	0.02	1.25	0.02	1.5	120	0	24	40	160	10
	BHCS-2	0	1.25	0	1.5	120	0	24	40	160	10

TABLE II: Grid parameters used in one BH test problem. The same conventions as in Table I are used.

For each boundary condition, the accuracy of our Poisson solver is examined comparing these solutions to the analytic ones.²

The Laplace equations (25) are solved from the surface integrals at the boundaries in our Poisson solver. The same equations (25) can be rewritten as

$$\nabla^2\psi = 0 \quad \text{and} \quad \nabla^2\alpha = -\frac{2}{\psi} f^{ij} \partial_i \psi \partial_j \alpha. \quad (35)$$

This form is also used to test the volume integral over the source in the Poisson solver.

In the next two sections $M_1/2$, $M_2/2$ refer to the radii of S_{i_1} and S_{i_2} of BHCS-1 and BHCS-2 correspondingly.

2. Convergence test for one black hole solution

First we treat the problem with no volume sources as in equations (25). In Fig. 4, the conformal factor ψ is plotted along the x-axis. BHCS-1 and 2 are centered on the x-axis at $x = 1.5$ and -1.5 respectively. In BHCS-1, we have two surface integrals, one at the inner (excision) boundary, S_{i_1} , with a radius $r_a = 0.02$ (in conformal geometry) and one at the outer boundary, S_{o_1} , at a distance $r_b = 1.25$. In the BHCS-2, there is no inner boundary sphere S_{i_2} ; we solve for the whole region inside S_{o_2} without any excised region. In this grid we need only to compute one surface integral at S_{o_2} . Finally CCS extends to a distance $r = 100$ and it excludes regions inside of two spheres I_1 and I_2 which are centered at $x = 1.5$ and $x = -1.5$ respectively and have radius 1.0. The overlapping region is one shell centered at $x = 1.5$ with $1.0 \leq r \leq 1.25$ and the corresponding one on the negative x-axis.

In Fig. 5, we show the fractional errors of the conformal factor shown in Fig. 4 for three different resolutions in table II. The error of α is of the same order. Since the terms calculated using 2nd order finite differencing, such

² In the above two black hole solution, the lapse α takes negative value in the neighborhood of each boundary sphere.

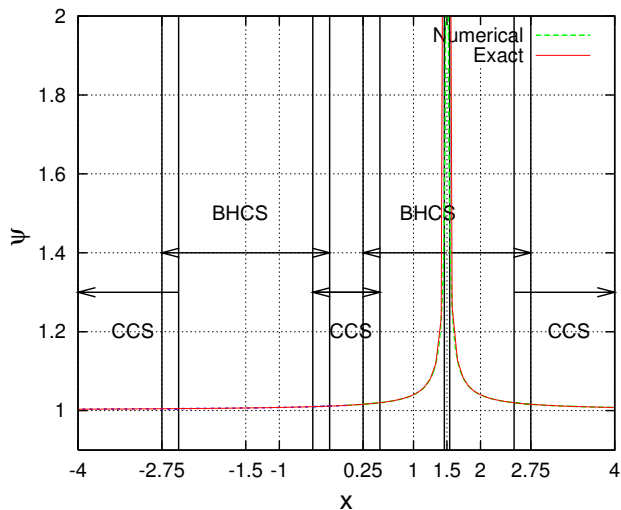


FIG. 4: Exact and numerical solution for ψ on the x-axis using the boundary condition (28)

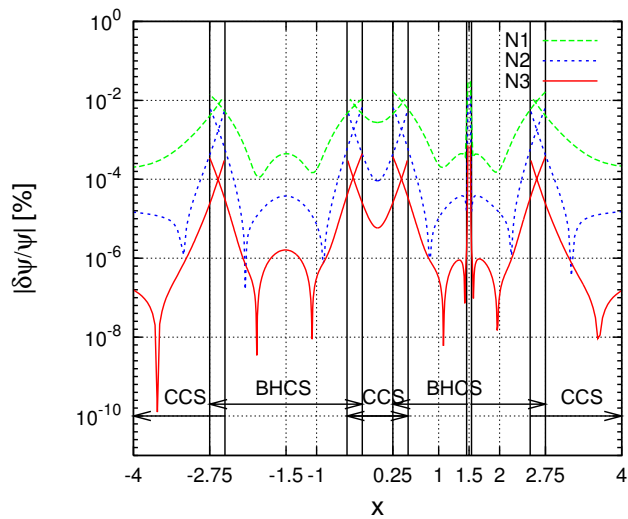


FIG. 5: Fractional errors of the conformal factor ψ , are plotted along the x-axis. Lines from top to bottom corresponds to the resolutions N1, N2, and N3 in Table II. Vertical lines are the boundaries of numerical domains.

as volume integrals, do not contribute in this solution, 4th-order convergence can be seen in Fig. 5 as expected.

Next we solve the same problem but in the form of (35). Near the inner boundary of BHCS-1, the source for the volume integral of the lapse, becomes very steep (approximately it goes as r^{-4}) and needs more grid points than the previous case in order to achieve the same order of error. For a grid set up as the one shown in Table III, the fractional errors of the lapse are shown in Fig. 6 where the no-boundary Green's function G^{NB} has been used. The error for the conformal factor is as in Fig. 5 since again we don't have any volume sources to integrate. For the same problem if we use the G^{DD} Green's

One black hole data with source											
Type	Coordinate	r_a	r_b	r_c	d	N_r	n_r	n_v	N_θ	N_ϕ	L
M1	CCS	0	100	3	—	80	40	—	20	80	10
	BHCS-1	0.02	1.25	1.0	1.5	120	112	8	10	40	5
	BHCS-2	0	1.25	0	1.5	30	0	6	10	40	5
M2	CCS	0	100	3	—	160	80	—	40	160	10
	BHCS-1	0.02	1.25	1.0	1.5	240	224	16	20	80	10
	BHCS-2	0	1.25	0	1.5	60	0	12	20	80	10
M3	CCS	0	100	3	—	320	160	—	80	320	10
	BHCS-1	0.02	1.25	1.0	1.5	480	448	32	40	160	10
	BHCS-2	0	1.25	0	1.5	120	0	24	40	160	10

TABLE III: Grid parameters used in one BH test problem with source. The same conventions as in Table I are used.

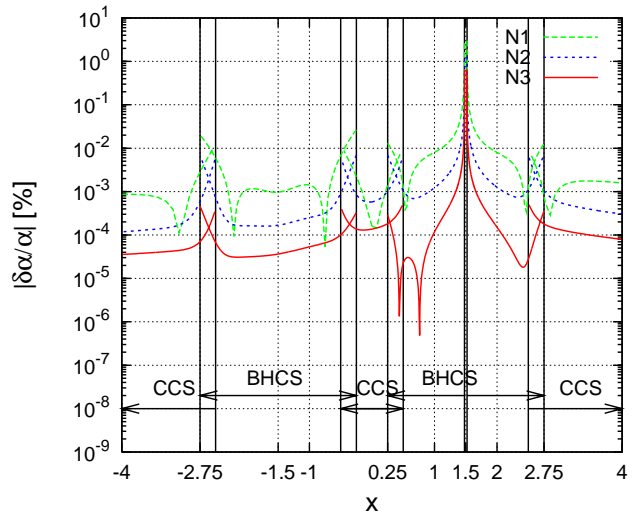


FIG. 6: Fractional errors of the lapse α , are plotted along the x-axis. Lines from top to bottom corresponds to the resolutions N1, N2, and N3 in Table III. The no-boundary Green's function G^{NB} has been used.

function we get the fractional errors of Fig. 7. With this latter choice of the Green's function the error near the throat is much smaller. Also we need fewer iterations to achieve convergence.

3. Convergence test for binary black hole solution

The two black hole solution (30) is computed numerically solving either set of (25) or (35). In Fig. 8, we plot the fractional error, Eq. 23 for the lapse α computed from the first set of Eq. (25) using the no-boundary Green's function G^{NB} and Neumann boundary condition.

The integral form of the first set (25) involves solely the surface integrals of Eq. (12). Since the surface terms are calculated using 4th order finite differences, convergence of this order can be seen in Fig. 8 when the grid resolution is increased from T1 to T3 in Table IV. Starting from $\alpha = \psi = 1$, the solution converges after 15 iterations with the convergence factor $c = 1.0$. Typical CPU time and memory to compute the 1/4 of the whole binary black

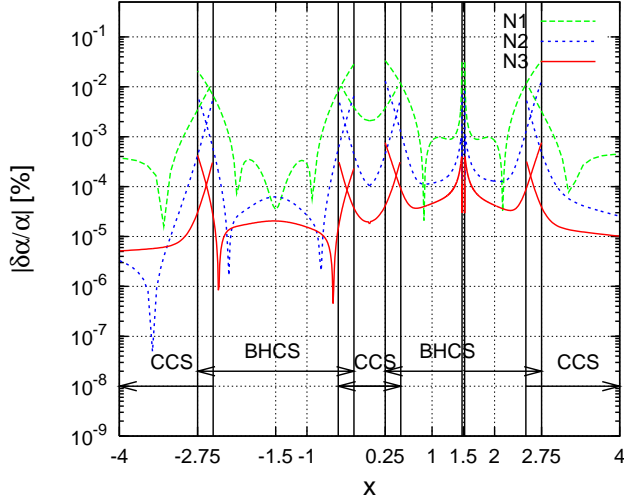


FIG. 7: Same as in Fig. 6, but now G^{DD} is used.

Two black hole data											
Type	Coordinate	r_a	r_b	r_c	d	N_r	n_r	n_v	N_θ	N_ϕ	L
T1	CCS	0	100	2.8	—	52	28	—	16	32	6
	BHCS-1	0.1	1.2	1.0	1.4	32	30	2	16	32	10
T2	CCS	0	100	2.8	—	104	56	—	32	64	10
	BHCS-1	0.1	1.2	1.0	1.4	64	60	4	32	64	10
T3	CCS	0	100	2.8	—	208	112	—	64	128	10
	BHCS-1	0.1	1.2	1.0	1.4	128	120	8	64	128	10

TABLE IV: Grid parameters used in two BH test problem. The same conventions as in Table I are used.

hole region is tabulated in Table V.

In Fig. 9, the fractional error (23) of the solution to Eq. (35) is shown for a different choice of the Green's functions for BHCS. The numerical integration in radial direction, that appears in the volume integrals of (12) are calculated with 2nd order accurate mid-point rule. In all test problems, we found that the largest error appears in computing α with Neumann boundary condition shown in Fig.9 bottom panel. However, even for this case, the error is controlled to give a fractional error less than 0.01% everywhere, when the highest resolution T3 is used. We have tested different combinations of the Green's functions with boundary conditions, and found

Type	CPU time/iteration [s]	Memory [MB]
T1	0.14	25
T2	1.0	73
T3	8.6	236

TABLE V: Typical CPU time and memory used for the BH calculations. The use of equatorial and π rotation symmetries reduce the number of grid points indicated in Table IV by a factor of 4. Note that the computational costs approximately scale linearly with respect to the total number of grid points which is $2^3 = 8$ times at each level T1-T3. Opteron 2 GHz with Portland fortran compiler is used.

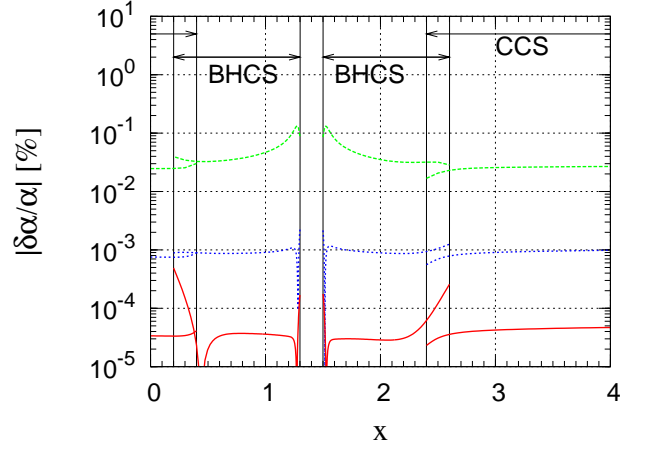


FIG. 8: Fractional error of the lapse is plotted along the x-axis. Lines from top to bottom correspond to the resolutions T1, T2, and T3 in Table IV. A set of Eq. (25) is solved using the no-boundary Green's function and by imposing Neumann boundary conditions. Vertical lines correspond to the boundaries of the numerical domains.

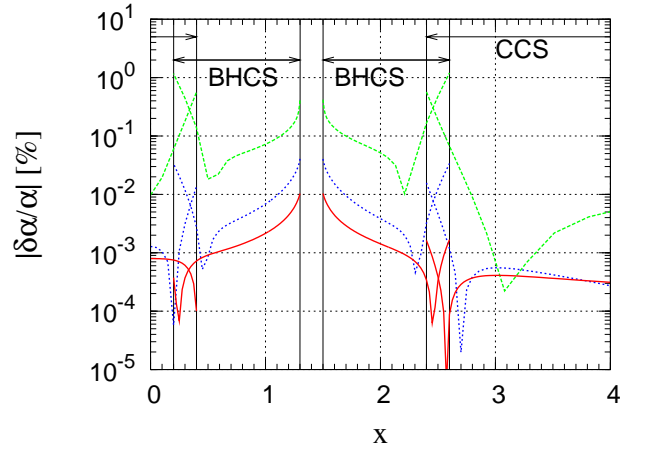
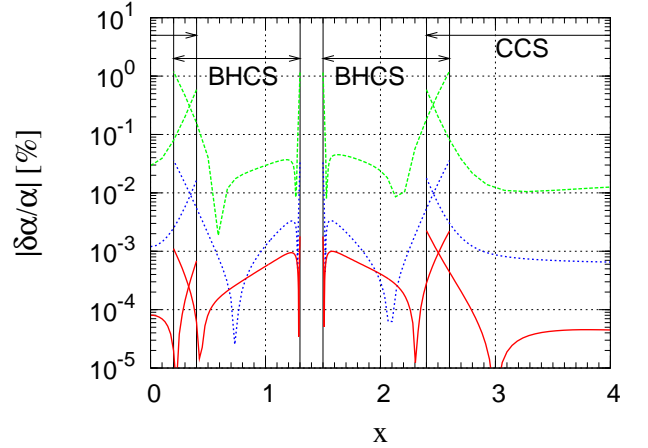


FIG. 9: Same as Fig. 8, but for Eq. (35). For the BHCS, G^{DD} is used in the top panel and G^{ND} in the bottom panel.

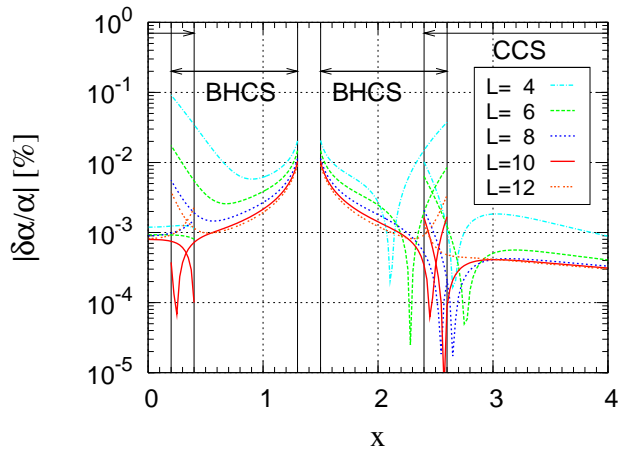


FIG. 10: Fractional errors of the lapse α are plotted along the x -axis for different values of the highest multipole in the Green's function. A set of Eq. (35) is solved using the Green's function G^{ND} with resolution T3 in Table IV.

similar or better convergence results. (The fractional error of the conformal factor ψ , on the other hand, scales in 4th order since the equation for ψ does not involve the volume integrals.)

Finally, the convergence test for the number of multipoles summed in the Green's function, L , with a fixed resolution (T3 in Table IV), is shown in Fig.10. Changing L from 4 to 12, convergence is achieved around $L = 10$. This is a dramatically small number compared to the binary neutron star case [21], for which $L = 30 \sim 40$ multipoles are required because only one domain (corresponding to CCS here) was used for computing the gravitational fields.

V. AN EXAMPLE FOR BINARY BLACK HOLE INITIAL DATA

To conclude the test for our new numerical code, we show an example of binary black hole initial data; a binary black hole solution of IWM formulation. This is to demonstrate that our new code can produce the binary black hole initial data with nonzero angular momentum, and locate the apparent horizon using the method described in Appendix A at the same time. Writing the spatially conformally flat metric

$$ds^2 = -\alpha^2 dt^2 + \psi^4 f_{ij}(dx^i + \beta^i dt)(dx^j + \beta^j dt), \quad (36)$$

in a chart $\{t, x^i\}$, the 5 metric potentials, the conformal factor ψ , the shift β^a and the lapse α are solved from the Hamiltonian constraint, momentum constraint and the spatial trace of the Einstein's equation, respectively. As shown in Appendix C, all these equations are written in elliptic form.

At the black hole excision boundary, certain Dirichlet data is imposed to ensure that the apparent horizon

Type	r_a	ψ_B	α_B	Ω	Ω_B
B1	0.1	3.0	1.0	0.3	0.0

TABLE VI: Parameters for the boundary conditions. Except for the value of r_a , the parameter set of T3 in Table IV is used for the computation.

appears outside of the boundary sphere. For simplicity, we do not intend to impose certain physically motivated boundary conditions (see below). Dirichlet boundary conditions are given to all variables $\{\psi, \alpha, \beta^a\}$ as

$$\psi = \psi_B = \text{constant}, \quad (37)$$

$$\alpha = \alpha_B = \text{constant}, \quad (38)$$

$$\beta^a = -\Omega \phi_C^a - \Omega_B \phi_B^a, \quad (39)$$

at the excision sphere $r = r_a$ of BHCS. For the boundary value of the conformal factor ψ_B , a constant is chosen large enough to form apparent horizons near the excision spheres. For the lapse α_B , we also assign a constant value. The boundary condition for the shift vector assigns a momentum and a spin to each hole. Here, ϕ_C^a and ϕ_B^a are the basis of ϕ coordinate of CCS and BHCS, respectively.

In Figs. 11 and 12, we show a solution with the boundary parameters shown in Table VI. All potentials are smoothly joined across the overlap of CCS and BHCS. In Fig.12, thick dotted circles right outside of the excised sphere (thin black circles) are the apparent horizons located using the method in the Appendix A.

VI. DISCUSSION

The KEH iteration using the Green's formula Eq. (12) is applicable to solve various types of partial differential equations with nonlinear sources. For example, this method has been applied to solve the helically symmetric scalar field and binary neutron stars [29]. In this work, the equation for the scalar field is written in the form of Helmholtz equation, and the half-advanced + half-retarded Green's function is used in Eq. (12) to compute a standing wave solution iteratively. We plan to compute the helically symmetric binary black hole/neutron star solution using the coordinate systems and iteration scheme presented in this paper.

Black hole singularities on an initial hypersurface are avoided either by excising a numerical domain in the neighbourhood of the singularities, or by using punctures. In the previous Sec. V, we applied rather crude boundary conditions at the black hole excision sphere. For physically motivated excision conditions, one imposes apparent horizon or isolated horizon boundary condition to the conformal factor at the excised sphere so as these spheres become automatically horizons [30, 31]. Alternatively one can use the puncture method to produce accurate initial data as the ones used in binary black holes evolutions [4, 5, 6, 7, 8], and black hole/neutron star binary simulations [32].

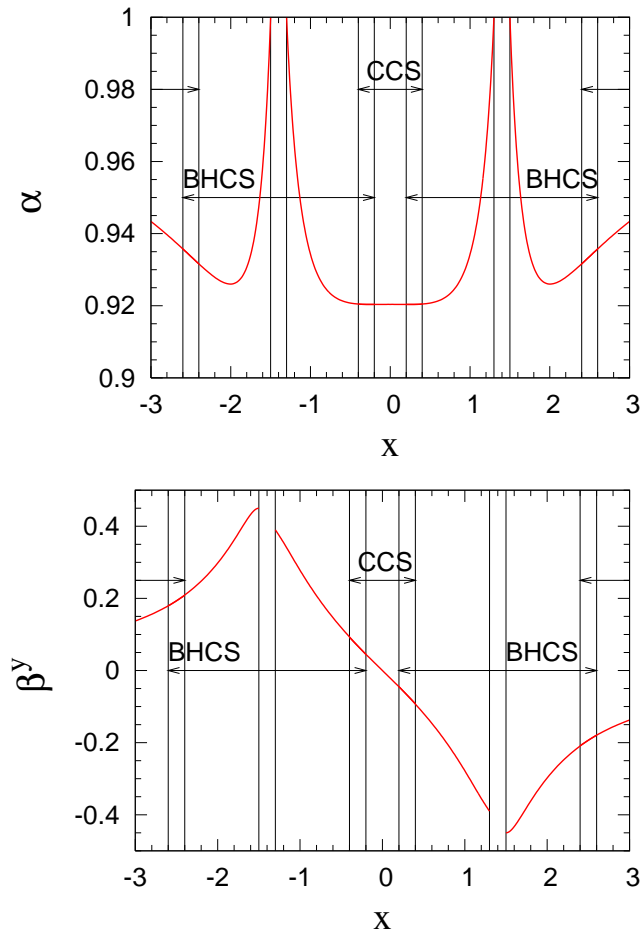


FIG. 11: Plots for α (top) and β^y (bottom) along the x -axis which pass through the excised region of the two holes. Vertical lines are the boundaries of each computational domain.

Acknowledgments

It is a pleasure to thank Spiros Cotsakis and Masaru Shibata for helpful discussions. Especially we would like to thank John L. Friedman for warm and continuous encouragement, and for providing the key idea of overlapping grids together with the argument of Appendix D. This work was supported by NSF grants PHY0071044, PHY0503366, as well as the joint Greek Ministry of Education and European Union research grant "Pythagoras" No. 1351.

Note added in proof.—Independently to our work, a new apparent horizon solver was developed recently using the same formulation by Lap-Ming Lin and Jerome Novak [37].

APPENDIX A: APPARENT HORIZON SOLVER

A method for locating the apparent horizon is described in this Appendix. Our method is a modification

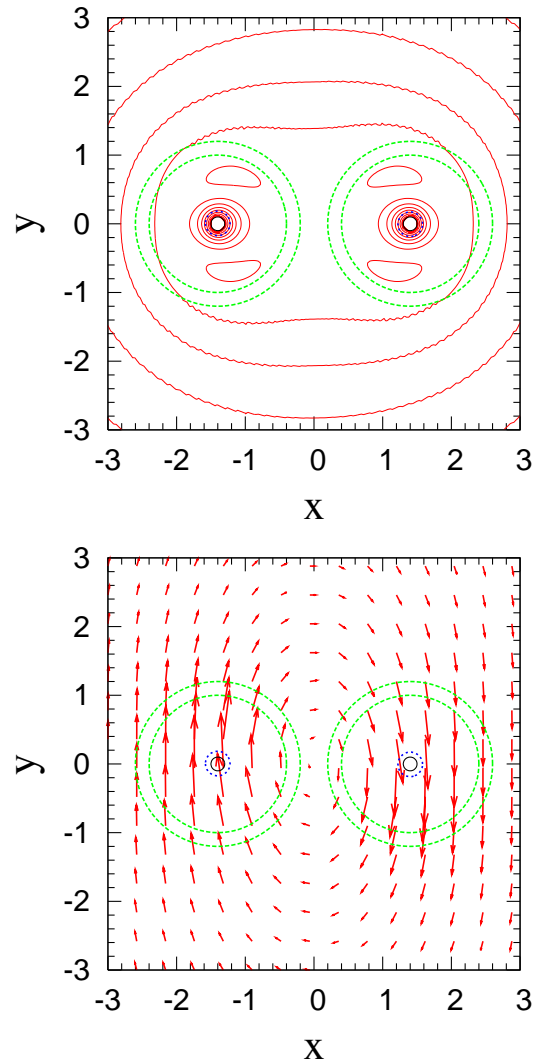


FIG. 12: Contours of the lapse α (top) and the vector field of the shift β^α (bottom) for the same model as Fig.11. Thick dotted circle in each figure is the apparent horizon.

of [33] and it will be one of the simplest apparent horizon finders without any symmetry restriction. For other works on apparent horizon finders, see e.g. [34, 35] and references therein.

An apparent horizon \mathcal{A} is defined as the boundary of all trapped regions on a spacelike hypersurface Σ , where the expansion ϑ of the outgoing null congruence ℓ^α orthogonal to \mathcal{A} vanishes. Introducing a null foliation \mathcal{H}_u whose normal is ℓ^α , where u labels a family of null hypersurfaces, the apparent horizon \mathcal{A} is the intersection $\mathcal{A} = \mathcal{H}_0 \cap \Sigma$. To each two dimensional surface $\mathcal{H}_u \cap \Sigma$, the spatial unit normal vector s^a is associated, and the outgoing null vector field ℓ^α can be written with a function f , $\ell^\alpha = f(n^\alpha + s^\alpha)$, where n^α is a timelike normal to Σ . Then, writing a projection tensor onto a surface orthogonal to s^a as $e_{ab} = \gamma_{ab} - s_a s_b$, the expansion ϑ is

written

$$\vartheta = e^{\alpha\beta}\nabla_\alpha\ell_\beta = f(D_a s^a - e^{\alpha\beta}K_{\alpha\beta}) \quad (\text{A1})$$

Hence, the equation

$$D_a s^a - e^{ab}K_{ab} = 0, \quad (\text{A2})$$

is satisfied at the apparent horizon \mathcal{A} .

We introduce a family of level surfaces parametrized by a spherical coordinate surrounding a black hole in the form ,

$$F := r - R_h(\theta, \phi), \quad (\text{A3})$$

where $F = 0$ coincides with the apparent horizon.³ The spatial normal s^a is proportional to the gradient of F ,

$$s_a = \frac{D_a F}{\|DF\|}, \quad (\text{A4})$$

where the norm $\|DF\|$ is defined by

$$\|DF\| = \sqrt{\gamma^{ab}D_a F D_b F} \quad (\text{A5})$$

We rewrite Eq. (A2) as an elliptic equation for the level surfaces in the conformally related geometry. Introducing quantities weighted with the conformal factor, $e_{ab} := \psi^4 \tilde{e}_{ab}$, $K_{ab} := \psi^4 \tilde{K}_{ab}$, $s_a := \psi^2 \tilde{s}_a$, the norm (A5) is transformed

$$\|DF\| = \psi^{-2} \sqrt{\tilde{\gamma}^{ab} \tilde{D}_a F \tilde{D}_b F} = \psi^{-2} \|\tilde{D}F\| \quad (\text{A6})$$

and

$$\tilde{s}_a = \frac{\tilde{D}_a F}{\|\tilde{D}F\|}. \quad (\text{A7})$$

Multiplying Eq. (A2) by the factor $\psi^2 \|\tilde{D}F\|$, we obtain an elliptic equation for the apparent horizon, namely

$$\tilde{\Delta}F + \hat{S} = 0, \quad (\text{A8})$$

$$\hat{S} := \tilde{D}_a \ln \frac{\psi^4}{\|\tilde{D}F\|} \tilde{D}^a F - \psi^2 \|\tilde{D}F\| \tilde{K}_{ab} \tilde{e}^{ab}, \quad (\text{A9})$$

which is satisfied on the surface $r = R_h(\theta, \phi)$. Separating the Laplacian associated with the flat metric, $\mathring{\Delta}$, from $\tilde{\Delta}$ associated with the conformal metric, $\tilde{\gamma}_{ab}$, we have

$$\tilde{\Delta}F = \mathring{\Delta}F + h^{ab} \mathring{D}_a \mathring{D}_b F - \tilde{\gamma}^{ab} C_{ab}^c \mathring{D}_c F, \quad (\text{A10})$$

where the second and third terms have been moved to the right hand side. Defining

$$\mathring{\Delta}F = \frac{2}{r} - \frac{1}{r^2} \mathring{\Delta}_H R_h = -\frac{1}{R_h^2} (\mathring{\Delta}_H - 2) R_h, \quad (\text{A11})$$

$$\mathring{\Delta}_H := \frac{1}{\sin\theta} \frac{\partial}{\partial\theta} \left(\sin\theta \frac{\partial}{\partial\theta} \right) + \frac{1}{\sin^2\theta} \frac{\partial^2}{\partial\phi^2}, \quad (\text{A12})$$

the equation for the apparent horizon (A2) is rewritten

$$(\mathring{\Delta}_H - 2) R_h = S, \quad (\text{A13})$$

$$S := R_h^2 (\tilde{S} + \hat{S}), \quad (\text{A14})$$

$$\tilde{S} := -h^{ab} \mathring{D}_a \mathring{D}_b F + \tilde{\gamma}^{ab} C_{ab}^c \mathring{D}_c F. \quad (\text{A15})$$

Terms in \tilde{S} vanish for spatially conformal flat geometry.

We find a solution to Eq. (A13)

$$R_h(x) = -\frac{1}{4\pi} \int_H d^2x G(x, x') S(x'), \quad (\text{A16})$$

where the coordinates x here represents (θ, ϕ) , and the function $G(x, x')$ is given in terms of Legendre expansion,

$$G(x, x') = \sum_{\ell=0}^{\infty} \frac{2\ell+1}{\ell(\ell+1)+2} \sum_{m=0}^{\ell} \epsilon_m \frac{(\ell-m)!}{(\ell+m)!} \\ \times P_\ell^m(\cos\theta) P_\ell^m(\cos\theta') \cos m(\phi - \phi'). \quad (\text{A17})$$

The same discretization as in BHCS, and an iteration similar to KEH method are applied to Eq. (A16) (see Sec.III). The 4th order Lagrange formula is used for finite differencing the source and for numerical integration. The iteration converges typically in 30 iterations, whose CPU time is negligible in the computation of initial data.

APPENDIX B: MULTIPOLE EXPANSION OF THE GREEN'S FUNCTIONS OF THE LAPLACIAN.

In our Poisson solver (12) one must choose appropriate Green's functions to meet the boundary conditions imposed on each of the field variables. In this Appendix, we present explicit forms of those used in the preceding sections. They are the Green's function without boundaries, $G^{\text{NB}}(x, x')$, and two Green's functions with boundaries on two concentric spheres S_a and S_b at radius $r = r_a$ and $r = r_b$, where $r_a < r_b$; one of them imposes Dirichlet conditions on both S_a and S_b , $G^{\text{DD}}(x, x')$, and the other imposes Neumann condition on S_a and Dirichlet condition on S_b , $G^{\text{ND}}(x, x')$. All Green's functions, representing $G(x, x')$, are expanded in multipoles, in terms of the associated Legendre functions $P_\ell^m(\cos\theta)$ in spherical coordinates (r, θ, ϕ) ,

$$G(x, x') = \sum_{\ell=0}^{\infty} g_\ell(r, r') \sum_{m=0}^{\ell} \epsilon_m \frac{(\ell-m)!}{(\ell+m)!} \\ \times P_\ell^m(\cos\theta) P_\ell^m(\cos\theta') \cos m(\phi - \phi'), \quad (\text{B1})$$

where the coefficient ϵ_m is defined by

$$\epsilon_m = \begin{cases} 1, & \text{for } m = 0, \\ 2, & \text{for } m \geq 1, \end{cases} \quad (\text{B2})$$

and hence the difference appears in the radial part of the Green's function $g_\ell(r, r')$, [36].

³ The level surface F may not coincide with the intersection $\mathcal{H}_u \cap \Sigma$, except at \mathcal{A}

1. Green's function without boundary $G^{\text{NB}}(x, x')$

For the Green's function of the Laplacian without boundary $G^{\text{NB}}(x, x')$, the radial part $g_\ell^{\text{NB}}(r, r')$, is defined by

$$g_\ell^{\text{NB}}(r, r') := \frac{r_{<}^\ell}{r_{>}^{\ell+1}}, \quad (\text{B3})$$

where $r_{>} := \sup\{r, r'\}$, and $r_{<} := \inf\{r, r'\}$.

When the Green's function G^{NB} is applied to BHCS with two concentric boundary spheres S_a and S_b located at $r = r_a$ and r_b , respectively, the following values are used to evaluate surface integrals of Eq. (12),

$$g_\ell^{\text{NB}}(r, r_a) = \frac{r_a^\ell}{r_a^{\ell+1}}, \quad (\text{B4})$$

$$g_\ell^{\text{NB}}(r, r_b) = \frac{r_b^\ell}{r_b^{\ell+1}}, \quad (\text{B5})$$

and, since $\nabla'^a G^{\text{NB}}(x, x') dS'_a = \mp \partial_{r'} G^{\text{NB}} r'^2 dr' d\Omega'$,

$$\partial_{r'} g_\ell^{\text{NB}}(r, r_a) = \ell \frac{r_a^{\ell-1}}{r_a^{\ell+1}}, \quad (\text{B6})$$

$$\partial_{r'} g_\ell^{\text{NB}}(r, r_b) = -(\ell+1) \frac{r_b^\ell}{r_b^{\ell+2}}. \quad (\text{B7})$$

Note that the form of (B6) indicates that the Green's function G^{NB} does not pick up $\ell = 0$ mode of the Dirichlet data at the sphere S_a ($r = r_a$).

2. Green's function for the region between two concentric spheres with Dirichlet conditions, $G^{\text{DD}}(x, x')$

The Green's function $G^{\text{DD}}(x, x')$ is a solution of Eq. (11) in a region between two concentric spheres S_a and S_b with radius $r = r_a$ and $r = r_b$ ($r_a < r_b$) where Dirichlet conditions are imposed. Its radial part $g_\ell^{\text{DD}}(r, r')$ associated with the ℓ th mode is written

$$g_\ell^{\text{DD}}(r, r') = \left[1 - \left(\frac{r_a}{r_b} \right)^{2\ell+1} \right]^{-1} \frac{r_a^\ell}{r_b^{\ell+1}} \times \left[\left(\frac{r_{<}}{r_a} \right)^\ell - \left(\frac{r_a}{r_{<}} \right)^{\ell+1} \right] \left[\left(\frac{r_b}{r_{>}} \right)^{\ell+1} - \left(\frac{r_{>}}{r_b} \right)^\ell \right] \quad (\text{B8})$$

By construction $g_\ell^{\text{DD}}(r, r')$ vanishes on the two spheres S_a and S_b ,

$$g_\ell^{\text{DD}}(r, r_a) = 0, \quad (\text{B9})$$

$$g_\ell^{\text{DD}}(r, r_b) = 0. \quad (\text{B10})$$

The derivatives that are used to compute the surface integral in Eq. (12), are

$$\partial_{r'} g_\ell^{\text{DD}}(r, r_a) = \left[1 - \left(\frac{r_a}{r_b} \right)^{2\ell+1} \right]^{-1}$$

$$\times (2\ell+1) \frac{r_a^{\ell-1}}{r_b^{\ell+1}} \left[\left(\frac{r_b}{r} \right)^{\ell+1} - \left(\frac{r}{r_b} \right)^\ell \right], \quad (\text{B11})$$

$$\partial_{r'} g_\ell^{\text{DD}}(r, r_b) = - \left[1 - \left(\frac{r_a}{r_b} \right)^{2\ell+1} \right]^{-1} \times (2\ell+1) \frac{r_a^\ell}{r_b^{\ell+2}} \left[\left(\frac{r}{r_a} \right)^\ell - \left(\frac{r_a}{r} \right)^{\ell+1} \right], \quad (\text{B12})$$

at S_a and S_b , respectively.

3. Green's function for the region between two concentric spheres with Neumann and Dirichlet conditions, $G^{\text{ND}}(x, x')$

Similarly, $G^{\text{ND}}(x, x')$, is the Green's function between S_a and S_b , where Neumann data are imposed on S_a and Dirichlet data are imposed on S_b . Its radial part $g_\ell^{\text{ND}}(r, r')$ associated with the ℓ th mode can be written

$$g_\ell^{\text{ND}}(r, r') = \left[1 + \frac{\ell}{\ell+1} \left(\frac{r_a}{r_b} \right)^{2\ell+1} \right]^{-1} \frac{r_a^\ell}{r_b^{\ell+1}} \times \left[\left(\frac{r_{<}}{r_a} \right)^\ell + \frac{\ell}{\ell+1} \left(\frac{r_a}{r_{<}} \right)^{\ell+1} \right] \times \left[\left(\frac{r_b}{r_{>}} \right)^{\ell+1} - \left(\frac{r_{>}}{r_b} \right)^\ell \right]. \quad (\text{B13})$$

The values of g_ℓ^{ND} at the surfaces S_a and S_b become

$$g_\ell^{\text{ND}}(r, r_a) = \left[1 + \frac{\ell}{\ell+1} \left(\frac{r_a}{r_b} \right)^{2\ell+1} \right]^{-1} \times \frac{2\ell+1}{\ell+1} \frac{r_a^\ell}{r_b^{\ell+1}} \left[\left(\frac{r_b}{r} \right)^{\ell+1} - \left(\frac{r}{r_b} \right)^\ell \right], \quad (\text{B14})$$

$$g_\ell^{\text{ND}}(r, r_b) = 0, \quad (\text{B15})$$

and its radial derivatives,

$$\partial_{r'} g_\ell^{\text{ND}}(r, r_a) = 0 \quad (\text{B16})$$

$$\partial_{r'} g_\ell^{\text{ND}}(r, r_b) = - \left[1 + \frac{\ell}{\ell+1} \left(\frac{r_a}{r_b} \right)^{2\ell+1} \right]^{-1} \times (2\ell+1) \frac{r_a^\ell}{r_b^{\ell+2}} \left[\left(\frac{r}{r_a} \right)^\ell + \frac{\ell}{\ell+1} \left(\frac{r_a}{r} \right)^{\ell+1} \right]. \quad (\text{B17})$$

The values of $\partial_{r'} g_\ell^{\text{ND}}(r, r_a)$ and $g_\ell^{\text{ND}}(r, r_b)$ vanish by construction.

APPENDIX C: 3+1 DECOMPOSITION FOR THE EINSTEIN EQUATIONS

In the usual (3+1) decomposition of the Einstein equations the spacetime metric is written as

$$ds^2 = g_{\alpha\beta} dx^\alpha dx^\beta$$

$$= -\alpha^2 dt^2 + \gamma_{ij}(dx^i + \beta^i dt)(dx^j + \beta^j dt) \quad (C1)$$

where $g_{\alpha\beta}$, γ_{ij} , are the 4D and 3D metrics, while α and β^i , are the lapse scalar and the shift vector respectively. The Riemannian 3-metric γ_{ij} on a hypersurface Σ is identified by the 4-tensor

$$\gamma_{\alpha\beta} = g_{\alpha\beta} + n_\alpha n_\beta \quad (C2)$$

where $n_\alpha = -\alpha \nabla_\alpha t$ is the unit future pointing normal to the hypersurface Σ . The indices of $\gamma_{\alpha\beta}$ can be raised either by $\gamma^{\alpha\beta}$ or by the full metric $g^{\alpha\beta}$ and that γ^α_β projects vectors onto the subspace orthogonal to n^α . Note that $g_{\alpha\beta}$ and $\gamma_{\alpha\beta}$ differ only on the time-time component while $g^{\alpha\beta}$ and $\gamma^{\alpha\beta}$ have identical only the space-space components ($g^{\alpha\beta}g_{\beta\gamma} = \delta^\alpha_\gamma$, $\gamma^{ij}\gamma_{jk} = \delta^i_j$, $\gamma^{\alpha\beta}\gamma_{\beta\gamma} \neq \delta^\alpha_\gamma$). The covariant components of the shift are $\beta_j = \gamma_{ij}\beta^i$ and the components on the normal vector are

$$n_\alpha = (\alpha, 0, 0, 0) \quad \text{and} \quad n^\alpha = \left(\frac{1}{\alpha}, \frac{-\beta^i}{\alpha}\right) \quad (C3)$$

The extrinsic curvature is

$$K_{\alpha\beta} = -D_\alpha n_\beta = -\gamma_{\alpha'}^{\alpha'} \gamma_{\beta'}^{\beta'} \nabla_{\alpha'} n_{\beta'} = -\frac{1}{2} \mathcal{L}_n \gamma_{\alpha\beta} \quad (C4)$$

where ∇ , D are the covariant derivatives associated with $g_{\alpha\beta}$ and $\gamma_{\alpha\beta}$ respectively. The Einstein equations can now be split into the constraint equations

$$\mathcal{R} - K_{ij}K^{ij} + K^2 = 16\pi\rho \quad (C5)$$

$$D_j(K^{ij} - \gamma^{ij}K) = 8\pi j^i \quad (C6)$$

and the evolution equations

$$\frac{\partial \gamma_{ij}}{\partial t} = -2\alpha K_{ij} + 2D_i\beta_j + 2D_j\beta_i \quad (C7)$$

$$\begin{aligned} \frac{\partial K_{ij}}{\partial t} = & \alpha \mathcal{R}_{ij} - D_i D_j \alpha + \alpha (K K_{ij} - 2K_{im} K_j^m) \\ & + K_{mi} D_j \beta^m + K_{mj} D_i \beta^m + \beta^m D_m K_{ij} \\ & - 8\pi \alpha \left(T_{ij} + \frac{1}{2} \gamma_{ij} (\rho - T_m^m) \right) \end{aligned} \quad (C8)$$

where $\rho = T_{\alpha\beta} n^\alpha n^\beta$ and $j^\alpha = -T_{\beta\gamma} n^\gamma \gamma^{\alpha\beta}$ are the energy and momentum density respectively as seen by an observer with four velocity n^α while \mathcal{R}_{ij} , \mathcal{R} , are the three dimensional Ricci tensor and Ricci scalar on the hypersurface Σ . From the two evolution equations we can find the time derivative of the trace of the extrinsic curvature

$$\partial_t K = \alpha \mathcal{R} - \Delta \alpha + \alpha K^2 + \beta_i D^i K - 8\pi \gamma^{ij} P_{ij} \quad (C9)$$

where $P_{ij} = T_{ij} + \frac{1}{2} \gamma_{ij} (\rho - T_m^m)$ are the source terms and $\Delta = D^i D_i$.

With a conformal transformation of the form

$$\gamma_{ij} = \psi^\lambda \tilde{\gamma}_{ij} \quad (C10)$$

the Ricci tensor becomes

$$\begin{aligned} R_{ij} = & \frac{\lambda(\lambda+2)}{4\psi^2} \tilde{D}_i \psi \tilde{D}_j \psi - \frac{\lambda(\lambda-2)}{4\psi^2} \tilde{\gamma}_{ij} \tilde{D}^m \psi \tilde{D}_m \psi \\ & - \frac{\lambda}{2\psi} (\tilde{D}_i \tilde{D}_j \psi + \tilde{\gamma}_{ij} \tilde{D}^m \tilde{D}_m \psi) + \tilde{\mathcal{R}}_{ij} \end{aligned} \quad (C11)$$

and the Ricci scalar

$$R = \psi^{-\lambda} \tilde{\mathcal{R}} - \frac{\lambda(\lambda-4)}{2\psi^{\lambda+2}} \tilde{D}^i \psi \tilde{D}_i \psi - \frac{2\lambda}{\psi^{\lambda+1}} \tilde{D}^m \tilde{D}_m \psi. \quad (C12)$$

Now the Hamiltonian (C5) and the momentum constraint (C6) can be written as

$$\begin{aligned} \tilde{\Delta} \psi - \frac{\psi}{2\lambda} \tilde{\mathcal{R}} + \frac{\lambda-4}{4\psi} \tilde{D}_i \psi \tilde{D}^i \psi + \frac{\psi^{\lambda+1}}{2\lambda} K_{ij} K^{ij} \\ - \frac{\psi^{\lambda+1}}{2\lambda} K^2 = -\frac{8\pi\rho\psi^{\lambda+1}}{\lambda} \end{aligned} \quad (C13)$$

$$\begin{aligned} \tilde{D}_j K^{ij} + \frac{5\lambda}{2\psi} K^{ij} \tilde{D}_j \psi - \frac{\lambda}{2\psi^{\lambda+1}} K \tilde{\gamma}^{ij} \tilde{D}_j \psi \\ - \frac{1}{\psi^\lambda} \tilde{\gamma}^{ij} \tilde{D}_j K = 8\pi j^i. \end{aligned} \quad (C14)$$

\tilde{D}_k is the covariant derivative with respect to $\tilde{\gamma}_{ij}$ and $\tilde{\Delta} = \tilde{D}^i \tilde{D}_i$. Note also that $D_i \omega_j = \tilde{D}_i \omega_j - C_{ij}^m \omega_m$ and $C_{ij}^m = \frac{\lambda}{2\psi} (\delta_i^m \tilde{D}_j \psi + \delta_j^m \tilde{D}_i \psi - \tilde{\gamma}_{ij} \tilde{\gamma}^{mk} \tilde{D}_k \psi)$.

1. Field equations for the initial data

Since we are searching for quasi-equilibrium states we assume the existence of a Killing vector

$$\xi^\alpha = t^\alpha + \zeta^\alpha = \left(\frac{\partial}{\partial t}\right)^\alpha + \Omega \left(\frac{\partial}{\partial \phi}\right)^\alpha = (1, \zeta^i) \quad (C15)$$

where $\zeta^i = \Omega(\partial/\partial\phi)^i$, and Ω is a constant representing the orbital angular velocity. In the presence of ξ^α the spatial metric γ_{ij} and the extrinsic curvature K_{ij} satisfy

$$\mathcal{L}_\xi \gamma_{ij} = 0 \quad \text{and} \quad \mathcal{L}_\xi K_{ij} = 0. \quad (C16)$$

From the first equation of (C16) we get

$$\partial_t \gamma_{ij} + D_i \zeta_j + D_j \zeta_i = 0 \quad (C17)$$

thus the time derivative of the spatial metric is associated with the spatial derivative of the rotational vector ζ^i . With the help of the evolution equation of γ_{ij} , (C7) we can obtain an expression for the extrinsic curvature by eliminating the time derivative of the three metric and therefore cast the initial value equations in a form that has no time derivatives. We find

$$K_{ij} = \frac{1}{2\alpha} (D_i \omega_j + D_j \omega_i) \quad \text{and} \quad K = \frac{1}{\alpha} D_i \omega^i \quad (C18)$$

where $\omega_i = \beta_i + \zeta_i$ is the comoving shift. Since

$$K_{ij}K^{ij} = \frac{1}{4\alpha^2}(\mathbb{L}\omega)_{ij}(\mathbb{L}\omega)^{ij} + \frac{1}{3}K^2 \quad (\text{C19})$$

where

$$(\mathbb{L}\omega)_{ij} = D_i\omega_j + D_j\omega_i - \frac{2}{3}\gamma_{ij}D_m\omega^m \quad (\text{C20})$$

and $(\mathbb{L}\omega)_{ij}(\mathbb{L}\omega)^{ij} = (\tilde{\mathbb{L}}\tilde{\omega})_{ij}(\tilde{\mathbb{L}}\tilde{\omega})^{ij}$ the hamiltonian (C13) and momentum constraints (C14) are written

$$\begin{aligned} \tilde{\Delta}\psi &= \frac{\psi}{2\lambda}\tilde{\mathcal{R}} - \frac{\lambda-4}{4\psi}\tilde{D}_i\psi\tilde{D}^i\psi - \frac{\psi^{\lambda+1}}{8\lambda\alpha^2}(\tilde{\mathbb{L}}\tilde{\omega})_{ij}(\tilde{\mathbb{L}}\tilde{\omega})^{ij} \\ &+ \frac{\psi^{\lambda+1}}{3\lambda}K^2 - \frac{8\pi\rho\psi^{\lambda+1}}{\lambda} \end{aligned} \quad (\text{C21})$$

$$\begin{aligned} \tilde{\Delta}\tilde{\omega}^i &= -\frac{1}{3}\tilde{D}^i\tilde{D}_j\tilde{\omega}^j - \tilde{\mathcal{R}}^i{}_j\tilde{\omega}^j + \tilde{D}_j\ln\left(\frac{\alpha}{\psi^{3\lambda/2}}\right)(\tilde{\mathbb{L}}\tilde{\omega})^{ij} \\ &+ \frac{4\alpha}{3}\tilde{D}^iK + 16\pi\alpha\psi^\lambda j^i \end{aligned} \quad (\text{C22})$$

Also by using the fact that

$$\Delta\alpha = \psi^{-\lambda}\left(\tilde{\Delta}\alpha + \frac{\lambda}{2\psi}\tilde{D}_i\psi\tilde{D}^i\alpha\right) \quad (\text{C23})$$

we can rewrite equation (C9) in the conformal geometry as

$$\begin{aligned} \tilde{\Delta}\alpha &= -\frac{\lambda}{2\psi}\tilde{D}_i\psi\tilde{D}^i\alpha + \psi^\lambda\left(\frac{1}{4\alpha}(\tilde{\mathbb{L}}\tilde{\omega})_{ij}(\tilde{\mathbb{L}}\tilde{\omega})^{ij}\right. \\ &\left. + \frac{\alpha K^2}{3} + \tilde{\omega}^i\tilde{D}_iK + 4\pi\alpha(\rho + T)\right) \end{aligned} \quad (\text{C24})$$

For the binary black hole case, the sources ρ , T_{ij} and j^i vanish, and take $\lambda = 4$. Under these assumptions, our system of equations is

$$\tilde{\Delta}\psi = \frac{\psi}{8}\tilde{\mathcal{R}} - \frac{\psi^5}{32\alpha^2}(\tilde{\mathbb{L}}\tilde{\omega})_{ij}(\tilde{\mathbb{L}}\tilde{\omega})^{ij} + \frac{\psi^5}{12}K^2 \quad (\text{C25})$$

$$\begin{aligned} \tilde{\Delta}\alpha &= \psi^4\left(\frac{1}{4\alpha}(\tilde{\mathbb{L}}\tilde{\omega})_{ij}(\tilde{\mathbb{L}}\tilde{\omega})^{ij} + \frac{\alpha K^2}{3} + \tilde{\omega}^i\tilde{D}_iK\right) \\ &- \frac{2}{\psi}\tilde{D}_i\psi\tilde{D}^i\alpha \end{aligned} \quad (\text{C26})$$

$$\begin{aligned} \tilde{\Delta}\tilde{\omega}_i &= -\frac{1}{3}\tilde{D}_i\tilde{D}_j\tilde{\omega}^j - \tilde{\mathcal{R}}_{ij}\tilde{\omega}^j + \tilde{D}^j\ln\left(\frac{\alpha}{\psi^6}\right)(\tilde{\mathbb{L}}\tilde{\omega})_{ij} \\ &+ \frac{4\alpha}{3}\tilde{D}_iK \end{aligned} \quad (\text{C27})$$

$$\begin{aligned} &= -\tilde{\mathcal{R}}_{ij}\tilde{\omega}^j + \tilde{D}^j\ln\left(\frac{\alpha}{\psi^6}\right)(\tilde{\mathbb{L}}\tilde{\omega})_{ij} \\ &+ \tilde{D}_i\left(\frac{2}{\psi}\tilde{\omega}^j\tilde{D}_j\psi\right) - \frac{K}{3}\tilde{D}_i\alpha + \alpha\tilde{D}_iK \end{aligned} \quad (\text{C28})$$

$$\begin{aligned} &= -\tilde{\mathcal{R}}_{ij}\tilde{\omega}^j + \tilde{D}^j\ln\left(\frac{\alpha}{\psi^6}\right)(\tilde{\mathbb{L}}\tilde{\omega})_{ij} \\ &+ \tilde{D}_i\left(\frac{8}{\psi}\tilde{\omega}^j\tilde{D}_j\psi\right) - \frac{4K}{3}\tilde{D}_i\alpha + \tilde{D}_i\tilde{D}_j\tilde{\omega}^j \end{aligned} \quad (\text{C29})$$

In the momentum constraint, the last two expressions, equations (C28) and (C29), come from the fact that D_iK involves the second derivative of the comoving shift $\tilde{\omega}_i$ as follows

$$\tilde{D}_i\tilde{D}_j\tilde{\omega}^j = \alpha\tilde{D}_iK + K\tilde{D}_i\alpha - \tilde{D}_i\left(\frac{6}{\psi}\tilde{\omega}^j\tilde{D}_j\psi\right) \quad (\text{C30})$$

APPENDIX D: TOY MODEL FOR IMPROVEMENT OF CONVERGENCE BY OVERLAP REGION

To analyze the improvement of the rate of convergence achieved by the overlap region, we consider a simple model to calculate the potential of a point mass M using two overlapping concentric spherical grids as shown in Fig. 13, bottom panel. The first grid extends from the coordinate center ($r = 0$) to the surface S_1 , and the second grid from S_2 to infinity (or practically to a large distance). In Fig. 13, top panel, there is no overlapping region, $S_1 = S_2 =: S$. The potential in region II Φ_{II} , can be calculated from the surface integral of the interface S_2 , as

$$\Phi_{\text{II}} = \frac{M + m}{r}, \quad (\text{D1})$$

where m is the error inherited from the initial guess for Φ given at the boundary S_2 . The potential of the region I Φ_{I} , is a sum of a volume and a surface integral at S_1 ,

$$\Phi_{\text{I}} = \frac{M}{r} + e. \quad (\text{D2})$$

Again e is the error inherited from the initial guess for Φ at S_1 . From continuity of potentials at S_1 , $\Phi_{\text{I}}(R_1) = \Phi_{\text{II}}(R_1)$, therefore

$$e = \frac{m}{R_1}, \quad (\text{D3})$$

$$\Phi_{\text{I}} = \frac{M}{r} + \frac{m}{R_1}. \quad (\text{D4})$$

The next step of iteration is to use this value to fix Φ_{II} . In region II, the potential at R_2 must satisfy $\Phi_{\text{II}}(R_2) = \Phi_{\text{I}}(R_2)$, whence

$$\Phi_{\text{II}} = \frac{M + m\frac{R_2}{R_1}}{r}. \quad (\text{D5})$$

Iterating this procedure n times, we will have

$$M^{(n)} = M + m\left(\frac{R_2}{R_1}\right)^n, \quad (\text{D6})$$

namely, the error after the n -th iteration is $m(R_2/R_1)^n$.

Analogously for the ℓ -th multipole component, writing the actual value as A , and the error in region II as a ,

$$\Phi_{\text{II}} = \frac{A + a}{r^{\ell+1}}. \quad (\text{D7})$$

The solution to region I will be

$$\Phi_I = \frac{A}{r^{\ell+1}} + Br^\ell, \quad (\text{D8})$$

where the second term is again an error. The boundary condition at R_1 , $\Phi_I(R_1) = \Phi_{II}(R_1)$ yields

$$B = \frac{a}{R_1^{2\ell+1}}, \quad (\text{D9})$$

and from continuity at R_2 , $\Phi_{II}(R_2) = \Phi_I(R_2)$,

$$\Phi_{II} = \frac{A + a \left(\frac{R_2}{R_1}\right)^{2\ell+1}}{r}. \quad (\text{D10})$$

Hence the higher multipole converges faster after the n -th iteration,

$$A^{(n)} = A + a \left(\frac{R_2}{R_1}\right)^{n(2\ell+1)}. \quad (\text{D11})$$

The boundaries S_1 and S_2 are used to communicate the information of the physical boundary conditions imposed at the asymptotic region, and the inner excision boundary, as well as the source from each region to the other. At the n -th step of iteration, the values of $\Phi(x')$ and $\partial\Phi(x')/\partial r'$ in the surface integrals in Eq. (12) are calculated from the potential of $(n-1)$ step of the iteration.

It is possible to achieve communication between the two regions without the overlap region, by mixing the values of the potentials Φ_I and Φ_{II} of the two regions. This is done when we calculate the value of $\partial\Phi(x')/\partial r'$ at the boundary as shown in the top panel of Fig. 13, choosing say the values at grids x_3, x_2, y_1, y_2, y_3 . In this way convergence to a correct solution is again obtained, but the number of iterations increases approximately ten times, even for simple toy problems presented in Sec.IV.

In the actual binary calculation shown in Fig. 2, when the values of Φ and $\partial\Phi(x')/\partial r'$ on S_{o_1} , are interpolated from CCS, some of these points do not belong to the computational domain of CCS. The smaller the overlapping region the more of these points exist. (For example at the point A in Fig. 2, when we interpolate the nearby CCS points we find that the point in the lower left corner does not belong to CCS.) In such case we interpolate the nearby BHCS points to find the value of the potential.

APPENDIX E: CONVERGENCE OF THE ITERATION

In section IIB we have said that a requisit of the Green's function for the KEH iteration to achieve convergence is that all multipole components of $\nabla'^a G(x, x')$ should not vanish at the boundary for solving Dirichlet problem, and similary $G(x, x')$ should not vanish for Neumann boundary conditions. In this Appendix we use the

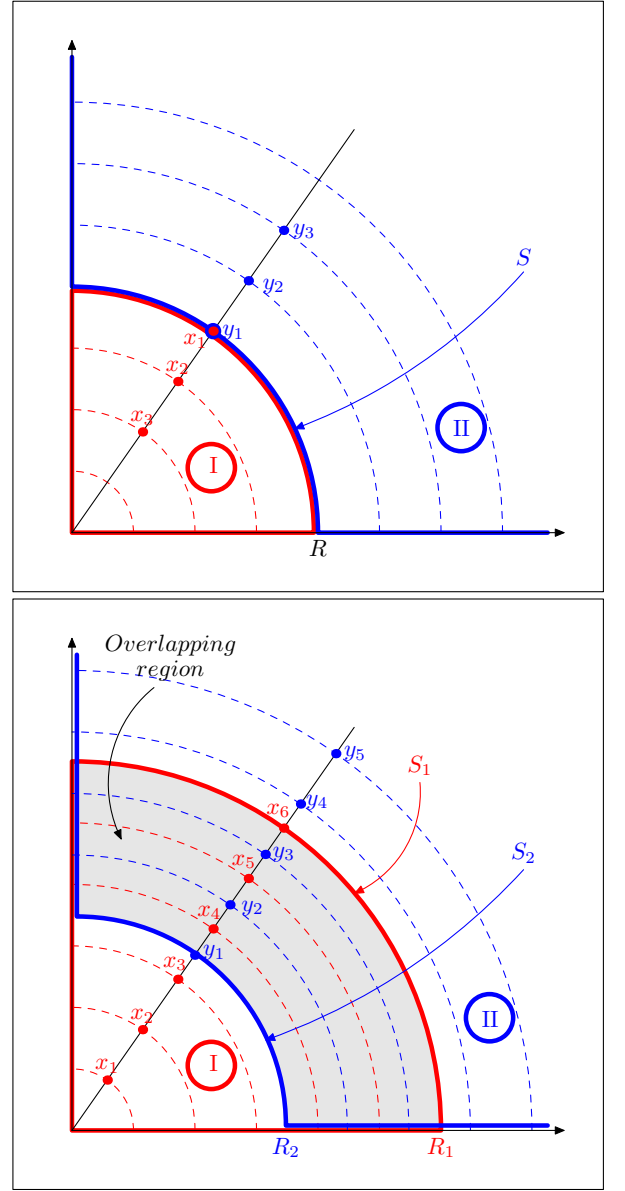


FIG. 13: Top, solving the poisson equation on two non overlapping grids. Bottom, solving the poisson equation by using two overlapping grids.

fixed point theorem to illustrate the convergence (or not) of the KEH method for simple spherically symmetric case with the flat Green's function.

Let's start with the following problem:

$$\nabla^2 \varphi = 0, \quad r \geq r_a \quad \text{with} \quad \frac{\partial \varphi}{\partial r} + \frac{\varphi}{2r} = 0 \quad \text{at} \quad r = r_a, \quad (\text{E1})$$

and $\lim_{r \rightarrow \infty} \varphi(r) = 1$, whose solution is $\varphi = 1 + r_a/r$. If we consider the map defined by

$$\Phi(\varphi) = \frac{1}{4\pi} \int_{S_a} \left[G(x, x') \frac{\partial \varphi}{\partial n'} - \varphi(x') \frac{\partial G}{\partial n'} \right] dS' \quad (\text{E2})$$

on a suitable Sobolev space, where S_a is the surface $r = r_a$, we can show the following:

claim: If $G(x, x') = \frac{1}{|x-x'|}$ and the functions $\varphi(r)$ satisfy $\frac{\partial\varphi}{\partial r} + \frac{\varphi}{2r} = 0$ on S_a then Φ has a fixed point. Indeed if φ_1 and φ_2 satisfy the above boundary condition so is $\varphi_1 - \varphi_2$ therefore

$$\begin{aligned} d(\Phi(\varphi_1), \Phi(\varphi_2)) &= \sup_r \{|\Phi(\varphi_1) - \Phi(\varphi_2)|\} \\ &\leq \frac{1}{2}d(\varphi_1, \varphi_2) \end{aligned} \quad (\text{E3})$$

where for the term with $\frac{\partial(\varphi_1 - \varphi_2)}{\partial n'}$ we used the boundary condition and for the term with $\varphi_1 - \varphi_2$ we used the fact that it depends only on r thus can be pulled out of the integral which when calculated gives zero. Therefore Φ has a fixed point which can be found if we take an initial value φ_0 and then compute the sequence $\{\varphi_n\}$ with $\varphi_{n+1} = \Phi(\varphi_n)$ (KEH method). By doing so and

adding the contribution from infinity which is 1.0 we get $\varphi_{n+1}(r) = 1 + \frac{r_a \varphi_n(r_a)}{2r}$ which tends to $1 + \frac{r_a}{r}$ as $n \rightarrow \infty$.

Now if we change the boundary condition to $\varphi = 0$ at $r = r_a$ the solution turns out to be $\varphi = 1 - r_a/r$. In this case the above argument breaks down and as we have seen the KEH iteration fails. The above argument gives us

$$d(\Phi(\varphi_1), \Phi(\varphi_2)) \leq r_a \left| \frac{\partial(\varphi_1 - \varphi_2)}{\partial r} \right|_{r=r_a}. \quad (\text{E4})$$

and nothing guaranties that Φ will have a fixed point any more. Actually $\varphi_{n+1}(r) = 1 - \frac{r_a^2}{r} \left(\frac{d\varphi_n}{dr} \right)_{r=r_a}$ thus starting from any constant value, the sequence is stuck at 1.0 and this explains why our code gives everywhere the value 1.0 with the Dirichlet boundary condition.

-
- [1] B. Brügmann, W. Tichy, and N. Jansen Phys. Rev. Lett. **92**, 211101 (2004)
- [2] M. Alcubierre et al., Phys. Rev. D. **72**, 044004 (2005).
- [3] F. Pretorius, Phys. Rev. Lett. **95**, 121101 (2005).
- [4] John G. Baker, Joan Centrella, Dae-Il Choi, Michael Koppitz, and James van Meter, Phys. Rev. Lett. **96**, 111102 (2006); John G. Baker, Joan Centrella, Dae-Il Choi, Michael Koppitz, and James van Meter, Phys. Rev. D **73**, 104002 (2006); James R. van Meter, John G. Baker, Michael Koppitz, and Dae-Il Choi, Phys. Rev. D **73**, 124011 (2006).
- [5] M. Campanelli, C. O. Lousto, Y. Zlochower, Phys. Rev. D **73**, 061501(R) (2006); M. Campanelli, C. O. Lousto, P. Marronetti, and Y. Zlochower Phys. Rev. Lett. **96**, 111101 (2006).
- [6] P. Diener, F. Herrmann, D. Pollney, E. Schnetter, E. Seidel, R. Takahashi, J. Thornburg, J. Ventrella, Phys. Rev. Lett. **96**, 121101 (2006).
- [7] F. Herrmann, D. Shoemaker, P. Laguna, gr-qc/0601026.
- [8] B. Brügmann, J.A. González, M. Hannam, S. Husa, U. Sperhake, and W. Tichy, preprint gr-qc/0610128.
- [9] T. Baumgarte, Phys. Rev. D. **62**, 024018 (2000).
- [10] H. P. Pfeiffer, S. A. Teukolsky, and G. B. Cook, Phys. Rev. D. **62**, 104018 (2000).
- [11] P. Marronetti and R. A. Matzner, Phys. Rev. Lett. **85**, 5500 (2000).
- [12] E.ourgoulhon, P. Grandclément, and S. Bonazzola, Phys. Rev. D. **65**, 044020 (2002); P. Grandclément, E.ourgoulhon, and S. Bonazzola, Phys. Rev. D. **65**, 044021 (2002).
- [13] G. Cook, Phys. Rev. D. **65**, 084003 (2002).
- [14] H. Pfeiffer, G. B. Cook, and S. Teukolsky, Phys. Rev. D. **66**, 024047 (2002)
- [15] W. Tichy, B. Brügmann, M. Campanelli, P. Diener, Phys. Rev. D **67**, 064008 (2003).
- [16] M. Ansorg, B. Brügmann, and W. Tichy, Phys. Rev. D **70**, 064011 (2004); M. Ansorg, Phys. Rev. D **72**, 024018 (2005).
- [17] Hwei-Jang Yo, J. Cook, S. Shapiro, T. Baumgarte, Phys. Rev. D. **70**,084033 (2004); Erratum *ibid.* **70** 089904 (2004)
- [18] M. Hannam, Phys. Rev. D. **72**, 044025 (2005).
- [19] G. B. Cook, Living Rev. Relativity **3**, 1 (2000).
- [20] H. Komatsu, Y. Eriguchi, and I. Hachisu, MNRAS **237**, 355 (1989).
- [21] K. Uryū and Y. Eriguchi, Phys. Rev. D. **61**, 124023 (2000); K. Uryū, M. Shibata and Y. Eriguchi, Phys. Rev. D. **62**, 104015 (2000).
- [22] J. W. York, Jr., in *Sources of Gravitational Radiation*, edited by L. Smarr (Cambridge, Cambridge, 1979), pp. 83-126.
- [23] J. Isenberg, Waveless Approximation Theories of Gravity, preprint (1978), University of Maryland; J. Isenberg and J. Nester, in *General Relativity and Gravitation Vol.1*, edited by A. Held, (Plenum Press, New York 1980).
- [24] J. R. Wilson and G. J. Mathews, Phys. Rev. Lett. **75**, 4161 (1995); P. Marronetti, G. J. Mathews and J. R. Wilson, Phys. Rev. D **60**, 087301 (1999).
- [25] T. W. Baumgarte, G. B. Cook, M. A. Scheel, S. L. Shapiro and S. A. Teukolsky, Phys. Rev. D **57**, 6181 (1998); *ibid* **57**, 7299 (1998).
- [26] M. Shibata, K. Uryū, and J. L. Friedman, Phys. Rev. D **70**, 044044 (2004); Erratum *ibid.* **70**, 129901(E) (2004).
- [27] J. M. Bowen, and J. W. York, Phys. Rev. D **21**, 2047 (1980).
- [28] D. R. Brill and R. W. Lindquist, Phys. Rev. **131**, 471 (1963).
- [29] S'i. Yoshida, B. C. Bromley, J. S. Read, K. Uryū, and J. L. Friedman, Classical Quantum Gravity **23**, S599 (2006).
- [30] J.L. Jaramillo, E.ourgoulhon, G.A. Mena Marugan, Phys. Rev. D **70**, 124036 (2004); E.ourgoulhon, J.L. Jaramillo, Phys.Rept., 423, 159, (2006).
- [31] G. B. Cook, H. P. Pfeiffer, Phys.Rev. D **70**, 104016, (2004).
- [32] M. Shibata, K. Uryū, Phys. Rev. D **74**, 121503(R) (2006); astro-ph/0611522 [Classical Quantum Gravity (to be published)].
- [33] T. Nakamura, Y. Kojima, and K.-I. Oohara, Phys. Lett. A, **106**, 235, 1984; K.-I. Oohara, T. Nakamura, and Y. Kojima, Phys. Lett. A, **107**, 452, 1985.
- [34] M. Shibata, Phys. Rev. D **55**, 2002 (1997); M. Shibata,

- and K. Uryū, Phys. Rev. D **62**, 087501 (2000).
- [35] J. Thornburg, Class. Quant. Grav., 21, 743 (2004).
- [36] J. D. Jackson, *Classical Electrodynamics*, Second Ed.,
(John Wiley & Sons, 1975).
- [37] Lap-Ming Lin and Jerome Novak, gr-qc/0702038.